Journal of Sound and Vibration 333 (2014) 3214–3235

Contents lists available at ScienceDirect

Journal of Sound and Vibration

journal homepage: www.elsevier.com/locate/jsvi

Sustained high-frequency energy harvesting through a strongly nonlinear electromechanical system under single and repeated impulsive excitations

Kevin Remick [a,*], Han Kyul Joo [d], D. Michael McFarland [b], Themistoklis P. Sapsis [d], Lawrence Bergman [b], D. Dane Quinn [c], Alexander Vakakis [a]

[a] Mechanical Science and Engineering, University of Illinois at Urbana-Champaign, 1206 W. Green Street, Urbana, IL 61801, USA
[b] Aerospace Engineering, University of Illinois at Urbana-Champaign, 104 S. Wright Street, Urbana, IL 61801, USA
[c] Mechanical Engineering, University of Akron, Akron, OH 44325, USA
[d] Mechanical Engineering, Massachusetts Institute of Technology, Cambridge, MA 02139, USA

ARTICLE INFO

Article history:
Received 29 July 2013
Received in revised form
13 January 2014
Accepted 10 February 2014
Handling Editor: M.P. Cartmell
Available online 25 March 2014

ABSTRACT

This work investigates a vibration-based energy harvesting system composed of two oscillators coupled with essential (nonlinearizable) stiffness nonlinearity and subject to impulsive loading of the mechanical component. The oscillators in the system consist of one grounded, weakly damped linear oscillator mass (primary system), which is coupled to a second light-weight, weakly damped oscillating mass attachment (the harvesting element) through a piezoelastic cable. Due to geometric/kinematic mechanical effects the piezoelastic cable generates a nonlinearizable cubic stiffness nonlinearity, whereas electromechanical coupling simply sees a resistive load. Under single and repeated impulsive inputs the transient damped dynamics of this system exhibit transient resonance captures (TRCs) causing high-frequency 'bursts' or instabilities in the response of the harvesting element. In turn, these high-frequency dynamic instabilities result in strong and sustained energy transfers from the directly excited primary system to the lightweight harvester, which, through the piezoelastic element, are harvested by the electrical component of the system or, in the present case, dissipated across a resistive element in the circuit. The primary goal of this work is to demonstrate the efficacy of employing this type of high-frequency dynamic instability to achieve enhanced nonlinear vibration energy harvesting under impulsive excitations.

1. Introduction

Long-lasting self-sustaining energy sources are becoming more important for wireless devices such as portable electronics and sensors. These devices typically rely on batteries, which must be frequently recharged or replaced. Battery charging or replacement can become complicated and sometimes impractical for wireless sensors, which are

* Corresponding author at: Department of Mechanical Sciences and Engineering, University of Illinois at Urbana-Champaign, 1416 Mechanical Engineering Laboratory, 1206 W. Green St., Urbana, IL 61801, USA. Tel.: +1 815 482 0661.
E-mail address: remick2@illinois.edu (K. Remick).

http://dx.doi.org/10.1016/j.jsv.2014.02.017
0022-460X

integrated into large structures in difficult-to-reach locations. A device that converts ambient mechanical vibration energy into usable electrical energy fulfills the self-sustaining requirement [1–3]. Piezoelectric materials are commonly used to convert mechanical energy to electrical energy so that ambient vibration can be harvested in a circuit [4,5]. The primary goal of this work is to study a methodology for enhancing the performance of these piezoelastic vibration-based energy harvesting systems through the use of nonlinear passive mechanical systems.

Many vibration-based energy harvesting systems are realized through either linear or weakly nonlinear oscillating systems. Linear systems require specific tuning to efficiently harvest energy when subjected to harmonic excitations, and are designed to match their natural frequency to the external forcing frequency [6,7]. When subject to proper tuning of the device parameters, linear energy harvesting systems efficiently transfer mechanical energy from environmental vibrations to a secondary attachment for subsequent conversion to electrical energy. In addition the electromechanical conversion process can be optimized by proper tuning of the electrical circuit parameters of the harvesting system [8–10,34–38]. This transfer of energy from the primary system to the secondary attachment is more profound for larger vibrational amplitudes and weaker system damping [11]. A sharp resonant peak is a fundamental characteristic of these linear systems with low damping. This is indicative of the narrowband nature of operation of these linear harvesting systems, and therefore their harvesting efficiency is expected to decrease significantly for excitation frequencies that vary only slightly from the tuned resonance frequency of the mechanical system. Harvesting of vibrations with time-varying frequency content using a linear single-degree-of-freedom harvester was theoretically studied in [33], and optimized harvesting strategies for this class of excitations were formulated.

Nonlinear energy harvesting systems have been proposed as a solution to frequency mistuning [10,12,13]. In [27] an analytical study of hybrid linear and nonlinear piezoelectric and electromagnetic energy harvesters was performed, whereas Mann et al. [28] examined the sensitivity of linear and nonlinear single-degree-of-freedom energy harvesters to parameter uncertainties. Erturk et al. [29] explored broadband nonlinear energy harvesting by piezo-magneto-elastic effects through magnetic bucking of an inverted cantilever beam and proved superior performance compared to systems without such buckling effects. Likewise, in recent works [30–32] the enhanced energy harvesting performance of bi-stable nonlinear energy harvesters to broadband excitation was shown. In another series of works it was proposed to use nonlinear mechanical attachments rather than linear attachments to a primary system, in which cubic nonlinearity in the elastic force was utilized to broaden the frequency response range of larger amplitude solutions [14,15]. This class of strong nonlinearity is referred to in the literature as essential (nonlinearizable) nonlinearity. The phenomenon of targeted energy transfer (TET) has been observed in these strongly nonlinear systems, in which TET describes the nearly irreversible passive transfer of substantial energy from the primary system to the nonlinear attachment [16–18]. The capability of the essentially nonlinear attachment to engage in resonance captures with modes of the linear structure over an extensive frequency and energy range results in complex dynamics of these systems [23]. The dynamics of the underlying Hamiltonian system possess highly degenerate eigenstructures with pairs of complex conjugate imaginary and multiple zero eigenvalues, resulting in these complex dynamics. Chaotic motions and dynamic instabilities result from high co-dimensional bifurcations in the nonlinear dynamics. These dynamic instabilities result in large relative displacements, which is ideal for piezoelastic energy harvesting.

It has been shown that nonlinear instabilities occur in highly degenerate systems associated with geometric stiffness [15] or damping [19] nonlinearities. This instability is characterized as a buildup of the response of a nonlinear attachment as it engages in a resonance capture with one of the modes of the linear oscillator. Another interesting dynamical phenomenon described in [19,20] is a peculiar damped transition into a state of sustained nonlinear resonance scattering in a system of two coupled oscillators with essential cubic stiffness nonlinearity. This transition was realized for weak viscous damping and only in the neighborhood of the low-frequency branch of the *impulsive orbit manifold* – (*IOM*) of the underlying Hamiltonian system. For a Hamiltonian system of two coupled oscillators with essential stiffness nonlinearity, an IOM consists of a countable infinity of periodic orbits and an uncountable infinity of quasi-periodic orbits, extending over broad frequency and energy ranges [21]. Impulsive forces applied to the linear oscillator with the system initially at rest enable these transitions, which take the form of nonlinear beats.

The present work seeks to extend the aforementioned results and apply them to the optimization of a nonlinear vibrational energy harvesting system subject to impulsive excitation. We show that sustained high-frequency dynamical instability can be realized in strongly nonlinear systems of coupled oscillators, which is in contrast to previous results in [15,19] where only low-frequency dynamic instabilities were reported. We also show that efficient energy harvesting can result for a single impulse and for a series of periodic impulses by activation of high-frequency dynamic instabilities due to high-frequency transient resonance captures of the dynamics. Finally, we present a strong argument for energy harvesting robustness of this system by investigation of optimal circuit and electromechanical coupling parameters, and studying the sensitivity of energy harvesting effectiveness to parameter variations.

The following analysis is restricted to excitations of the linear (primary) system to represent vibrations in physical bodies in nature, e.g. bridges or buildings. While these physical bodies are truly nonlinear in nature, they are predominantly linear systems, or can be linearized. Strongly nonlinear primary systems are not considered in this work because these physical systems are not the targeted application for this type of energy harvester.

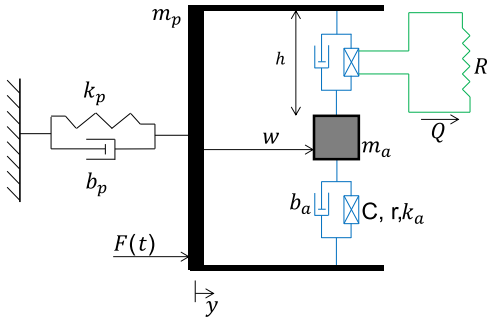

Fig. 1. Model of the nonlinear energy harvesting system (electric circuit shown only for half of the piezoelastic cable).

2. Modeling and measures of harvesting efficiency

We consider an energy harvesting system composed of a linear damped oscillator (denoted as the 'primary system') attached to a secondary lightweight mass (denoted as the 'harvester') through a piezoelastic cable (cf. Fig. 1). The cable is modeled as a piezoelectric element in series with a linear spring (modeling the linear elasticity of the cable), with the resulting combination in parallel with a linear viscous damper (modeling the dissipative forces in the cable). As a result, the transmitted forces across the linear spring and piezoelectric element of the cable are equal, and denoted by F_s, and the force exerted by the linear viscous damper is symbolized by F_d. Denoting by z_1 and z_2 the axial displacements across the linear spring and the piezoelectric element, respectively, the force F_s is expressed as

$$F_s = k_1 z_1 = k_2 z_2 - \left(\frac{k_{33}}{d(1-k_{33})}\right) Q \tag{1}$$

where k_1 and k_2 denote the axial stiffness of the spring and piezoelastic elements of the cable, respectively; d and k_{33} are piezoelectric coupling and electromechanical coupling parameters of the piezoelastic element, respectively, and are related to the constitutive law governing the elastic deformation and the generated charge; Q describes the electric charge in the piezoelectric element. The total force across the piezoelastic cable can be expressed in terms of $z = z_1 + z_2$ (the total stretch of the half-span of the cable) as

$$F_s = (k_a) z - (r k_a) Q \tag{2}$$

where $k_a = [k_1^{-1} + (1-k_{33}) k_2^{-1}]^{-1}$. Note that this represents a device-level constitutive law for the piezoelastic cable element. In terms of the piezoelectric material constants, the coupling parameter r represents the device-level piezoelectric voltage constant, expressed as

$$r = \frac{d}{\epsilon^T (A/l)}$$

where ϵ^T is a scalar parameter defining the permittivity material property, A denotes the cross section and l the unstretched length of the piezoelastic element (in this work it is assumed that $l = h$, where h is the half-length of the piezoelastic cable). Therefore the total axial force generated in the cable is

$$F = F_s + F_d = (k_a) z - (r k_a) Q + b_a \dot{z} \tag{3}$$

We note that even through the piezoelastic cable connecting the primary system with the harvester is assumed to obey a *linear* constitutive law (see Eq. (3)), its transverse deflection is expected to generate *strongly nonlinear* dynamics due to geometric/kinematic effects. Indeed, in terms of the relative displacement w of the harvester with respect to the primary system in the direction of the motion, the stretch in the cable and its time derivative are expressed by the strongly nonlinear relationships

$$z = \sqrt{w^2 + h^2} - l \;\Rightarrow\; \dot{z} = \frac{w\dot{w}}{\sqrt{w^2 + h^2}}$$

leading to the nonlinear equations of motion governing the oscillations of the primary system and the harvester

$$m_p \ddot{y} + b_p \dot{y} + k_p y - \left[b_a \frac{w\dot{w}}{w^2 + h^2} + k_a \left(\sqrt{w^2 + h^2} - l \right) - (r k_a) Q \right] \frac{2w}{\sqrt{w^2 + h^2}} = F(t)$$

$$m_a (\ddot{y} + \ddot{w}) + \left[b_a \frac{w\dot{w}}{w^2 + h^2} + k_a \left(\sqrt{w^2 + h^2} - l \right) - (r k_a) Q \right] \frac{2w}{\sqrt{w^2 + h^2}} = 0 \tag{4}$$

Here, y denotes the absolute displacement of the primary system, m_p and m_a the mass of the primary system and the harvester, k_p and b_p the stiffness and damping coefficients of the primary system, and $F(t)$ the external load applied to the primary system in the direction of the motion with the system being initially at rest.

To complete this set of equations we need to consider the electrical constitutive equation for the piezoelectric element, which can be written as

$$V = (1/C)Q - (rk_a)z$$

where C denotes capacitance, or in terms of w:

$$V = (1/C)Q - (rk_a)\left(\sqrt{w^2+h^2} - l\right)$$

Finally, assuming that the voltage across the piezoelectric element is harvested through a resistive load with resistance R, we can relate the harvested voltage to the rate of change of the charge by $V = R\dot{Q}$, and derive the final set of equations of motion describing the dynamics of the nonlinear harvesting device as

$$m_p\ddot{y} + b_p\dot{y} + k_p y - \left[b_a\frac{w\dot{w}}{w^2+h^2} + k_a\left(\sqrt{w^2+h^2} - l\right) - (rk_a)Q\right]\frac{2w}{\sqrt{w^2+h^2}} = F(t)$$

$$m_a(\ddot{y}+\ddot{w}) + \left[b_a\frac{w\dot{w}}{w^2+h^2} + k_a\left(\sqrt{w^2+h^2} - l\right) - (rk_a)Q\right]\frac{2w}{\sqrt{w^2+h^2}} = 0$$

$$R\dot{Q} + (1/C)Q - (rk_a)\left(\sqrt{w^2+h^2} - l\right) = 0 \tag{5}$$

We emphasize again that although all constitutive relations for the various elements of the system were assumed to be linear, the resulting equations of motion are strongly nonlinear due to geometric and kinematic effects. As shown in previous works [15,19,24], these types of strong nonlinearities can lead to interesting dynamic instabilities, which, as shown below can be utilized constructively for energy harvesting.

The principal aim of our study is to show that high-frequency dynamic instabilities in the response of system (5) generated by the strong nonlinearities can provide an effective mechanism for vibration energy harvesting. A preliminary nonlinear dynamic analysis performed in [24] has theoretically and experimentally demonstrated the efficacy of introducing sustained high-frequency dynamic instability in the same system but with the electric circuit (the harvester) removed, under single or sustained impulsive excitation. As shown in that work, under specific impulse excitations of the primary system the transient damped dynamics of the system tracks a *high-frequency IOM* in the frequency–energy plane. Dynamic instabilities arise at bifurcation points along damped transitions in the neighborhood of the IOM, causing bursts in the response of the lightweight attachment (the harvester) which resemble self-excited resonances. Moreover, for appropriate parameter designs the system remains in a state of sustained high-frequency dynamic instability under the action of repeated impulses. In turn, this sustained instability results in strong energy transfers from the directly excited primary system to the harvester, a feature that we intend to exploit in our energy harvesting application, with the addition of an electric circuit to the harvester.

As a first step in our study of the dynamics of the electromechanical harvesting system (5) we introduce non-dimensionalized variables and parameters by scaling the time variable as $t = c_t\tau$, the displacements as $w = c_y x$, $y = c_y u$, and the charge as $Q = c_Q q$, with the normalization coefficients defined by

$$c_t = (m_p/k_p)^{1/2}, \quad c_y = h(m_a k_p/m_p k_a)^{1/2}, \quad c_Q = (hm_a/2)(C/k_a)^{1/2}$$

Then the equations of motion are non-dimensionalized, and the nonlinear terms are expanded in Taylor series about $x = 0$, keeping terms only up to third order. This yields the set of simplified normalized equations given by

$$\ddot{x} + \lambda\dot{x} + x - \mu[\zeta u\dot{u} + (\sigma + u^2) - \beta q]u = f(\tau)$$

$$\ddot{x} + \ddot{u} + [\zeta u\dot{u} + (\sigma + u^2) - \beta q]u = 0$$

$$\rho\dot{q} + q - \beta(\sigma + u^2) = 0 \tag{6}$$

where $f(\tau) \equiv F(t(\tau))$, $(\dot{\cdot}) \equiv d/d\tau$, and the non-dimensional parameters are defined as

$$\lambda = b_p(k_p m_p)^{-1/2}, \quad \mu = m_a/m_p, \quad \zeta = 2(b_a/k_a)(k_p/m_p)^{1/2},$$

$$\sigma = 2(m_p k_a/m_a k_p)(1 - l/h), \quad \beta = r(Ck_a)^{1/2}, \quad \rho = RC(k_p/m_p)^{1/2}$$

Within these strongly nonlinear nondimensional equations of motion, the parameter μ represents the mass ratio between the harvester and the primary system, and λ the mechanical damping in the primary system. The mechanical damping in the harvester is given by $\mu\zeta$, and the (nondimensional) linear component of the restoring force in the harvester is $\mu\sigma$. For example, if the elastic component of the coupling piezoelastic cable is unstretched in the equilibrium configuration so that $u = 0$, then $\sigma = 0$. Finally, β characterizes the piezoelectric coupling between the mechanical and electrical components of the system, and ρ is the equivalent circuit of the electrical load. We aim to study the efficacy of using this nonlinear harvesting device under single and repetitive impulsive excitations of the primary system. To this end, we define certain energy measures.

Two different excitation scenarios will be considered in this work. In the first, the harvesting system (6) is initially at rest at $\tau = 0-$, and a single impulse $f(\tau) = I_0\delta(\tau)$ is applied to the primary system at $\tau = 0+$. Hence, the equations of motion (6) are complemented by the initial conditions:

$$x(0+) = 0, \quad \dot{x}(0+) = I_0, \quad u(0+) = 0, \quad \dot{u}(0+) = -I_0, \quad q(0+) = 0 \tag{7}$$

Recall that $\dot{u}(t)$ corresponds to the normalized relative velocity between the two oscillators; therefore, the relative velocity initial condition must be defined as above so that the initial velocity of the harvester is zero.

In the second excitation scenario the primary system is excited by a periodic series of identical impulses; i.e., by a pulse train. For the first impulse at $\tau = 0-$, we assume again that the system is at rest, so immediately after the application of the first impulse the initial conditions of system (6) are given by (7). Following the first impulse we define the impulsive period μ_T as the time between consecutive impulses, and the normalized impulsive period as the multiple n of the fundamental period $T_0 = 2\pi$ of the linear oscillator between consecutive impulses, $n = \mu_T/T_0$. For example, a normalized impulsive period of 5 would define a periodic pulse train, with the intensity of the impulse being equal to I_0 and applied to the primary system every 5 fundamental periods. In mathematical form the pulse train is defined as $f(\tau;\mu_T) = \sum_{k=0}^{N} I_0\delta(\tau - k\mu_T)$, where N denotes the total number of applied impulses after the first in the given excitation event. In this scheme, the pth impulse applied to the linear oscillator at $\tau = p\mu_T+$, $p \geq 1$, corresponds to the following initial conditions for system (6) immediately after the application of the pth impulse:

$$\begin{gathered} x(0+) = 0, \quad \dot{x}(0+) = I_0, \quad u(0+) = 0, \quad \dot{u}(0+) = -I_0, \quad q(0+) = 0 \\ x(p\mu_T+) = x(p\mu_T-), \quad \dot{x}(p\mu_T+) = \dot{x}(p\mu_T-) + I_0, \\ u(p\mu_T+) = u(p\mu_T-), \quad \dot{u}(p\mu_T+) = \dot{u}(p\mu_T-) - I_0, \\ q(p\mu_T+) = q(p\mu_T-), \quad p = 1, \ldots, N \end{gathered} \tag{8}$$

It follows that the initial state of the system will differ at each consecutive impulse, depending on the remaining vibration energy in the two coupled oscillators at the time of application of the pth impulse.

We now develop energy harvesting measures to quantify the efficiency of system (6) in later sections. Starting from the first excitation scenario corresponding to initial conditions (7), the total normalized energy in the system at an arbitrary time τ can be expressed as

$$E(\tau; I_0) = \overbrace{\overbrace{\left[\frac{\dot{x}^2 + x^2}{2}\right]}^{\text{Primary}} + \mu\overbrace{\left[(\dot{x} + \frac{\dot{u})^2}{2} + \frac{(\sigma + u^2)^2}{4}\right]}^{\text{Harvester}}}^{\text{Mechanical energy}} - \underbrace{\left[\frac{\mu\beta}{2} q(\sigma + u^2)\right]}_{\text{Coupling energy}} + \underbrace{\left[\frac{\mu}{4} q^2\right]}_{\text{Electrical energy}} \tag{9}$$

where the implicit dependence of the normalized energy on the impulse intensity I_0 was noted as a parameter in (9). The nondimensional power harvested through the resistive load is then given by

$$P_h(\tau; I_0) = \frac{\mu\rho}{2}(\dot{q})^2 \tag{10}$$

Using (10), the normalized energy harvested by the system in the normalized time interval $[\tau, \tau + T]$ is computed by

$$M(\tau, T; I_0) = \frac{1}{E(\tau; I_0)} \int_{\tau}^{\tau+T} P_h(u; I_0) du \tag{11}$$

which represents the energy harvested in the resistive load over an interval of time T, normalized by the total energy in the system at time τ. Again, the implicit dependence of the normalized harvesting measure (11) on the impulse intensity I_0 was noted. This is the basic energy harvesting measure that will be used in Section 4 to study the efficiency of system (6) under a single impulse excitation.

Considering now the second excitation scenario for initial conditions (8), we need to generalize measure (11), and develop harvesting measures suitably adapted to the physics of the problem of repetitive applied impulses. To this end, we first define a time-averaged energy harvested measure

$$M_1 = \frac{1}{T_{\text{total}}} \int_0^{T_{\text{total}}} P(\tau; I_0) d\tau = \frac{1}{T_{\text{total}}} \int_0^{T_{\text{total}}} \frac{\mu\rho}{2}(\dot{q})^2(\tau) d\tau \tag{12}$$

where T_{total} denotes the total time interval of the time series considered. Hence, M_1 represents the average rate of energy harvested per unit of normalized time. A second energy harvested measure is the impulse-averaged harvested energy, or the average energy harvested per impulse, defined as

$$M_2 = \frac{1}{N_{\text{impulses}}} \int_0^{T_{\text{total}}} P(\tau; I_0) d\tau = \frac{1}{N_{\text{impulses}}} \int_0^{N_{\text{impulses}}\mu_T} \frac{\mu\rho}{2}(\dot{q})^2(\tau) d\tau \tag{13}$$

where N_{impulses} denotes the number of impulses with the inter-arrival period μ_T taken into account. Finally, we define a third measure, namely the impulse-averaged canonical energy harvested, by

$$\overline{M_3} = \frac{1}{N_{\text{impulses}}} \sum_{i=0}^{N_{\text{impulses}}} M_3(i),$$

$$M_3(i) = \frac{2E_{\text{harv},\,i}}{(\dot{x}^2+x^2)\big|_{i\mu_T+} + \mu\left[(\dot{x}+\dot{u})^2+(\kappa/2)(\sigma+u^2)^2\right]\Big|_{i\mu_T+} - [\mu\beta q(\sigma+u^2)]\big|_{i\mu_T+} + \left[(\mu/2)q(i\mu_T+)^2\right]} \tag{14}$$

where $E_{\text{harv},\,i}$ is the energy harvested in the time period $i\mu_T < \tau < (i+1)\mu_T$, i.e., in the cycle of the harvester response following the application of the ith impulse. Hence, $\overline{M_3}$, represents the mean value of the total energy harvested over the total impulsive energy applied to the system. Equivalently, if $M_3(i)$ indicates the ratio of energy harvested in the cycle following the application of the ith impulse, the measure $\overline{M_3}$ defines the mean value of $M_3(i)$ for $0 < i < N_{\text{impulses}}$. These measures will be utilized in the study of energy harvesting of system (6) under repeated impulses, performed in Section 5.

As mentioned previously, our principal aim is to show that effective energy harvesting can be achieved by inducing sustained high-frequency dynamic instability of the lightweight harvester under single or repetitive impulsive excitation. To demonstrate the dynamic mechanism governing this instability, it is necessary to briefly consider the underlying Hamiltonian dynamics of system (6), and discuss the realization of a countable infinity of high-frequency transient resonance captures (TRCs). It is through the excitation of such high-frequency TRCs that conditions for effective nonlinear energy harvesting are realized.

3. Underlying Hamiltonian dynamics

We consider the underlying Hamiltonian system derived from the normalized equation (6) by setting $\lambda = \zeta = \beta = \rho = f(\tau) = 0$; i.e., by removing the damping, electrical and forcing terms, and by depicting its dynamics in a *frequency energy plot – FEP* [22,24]. This plot depicts branches of periodic and quasi-periodic orbits of the underlying Hamiltonian system at varying energy levels. When weak damping (or any other non-conservative term) is added to the equations of motion, transitions between different branches of the FEP can be realized by computing the wavelet transform spectra of the corresponding transient responses and superimposing the spectra on the Hamiltonian FEP. Such representations are based on the concept that the weakly non-conservative dynamic transitions are mainly influenced by the underlying Hamiltonian dynamics, with the non-conservative effects affecting transitions between branches in the FEP. This concept has been tested extensively in [22] and other works (e.g., [24]).

An example of an FEP for the underlying Hamiltonian system is depicted in Fig. 2 for parameters $\mu = 0.10$ and $\sigma = 0$. *Backbone branches* denoted by S11 $\pm$ correspond to in-phase and out-of-phase periodic orbits in 1:1 resonance, respectively, i.e., periodic orbits where the primary system and the harvester oscillated at the same fundamental frequency. *Subharmonic tongues*, such as S13 and S15 in Fig. 2, correspond to subharmonic 1:3 and 1:5 resonances, respectively, between the primary

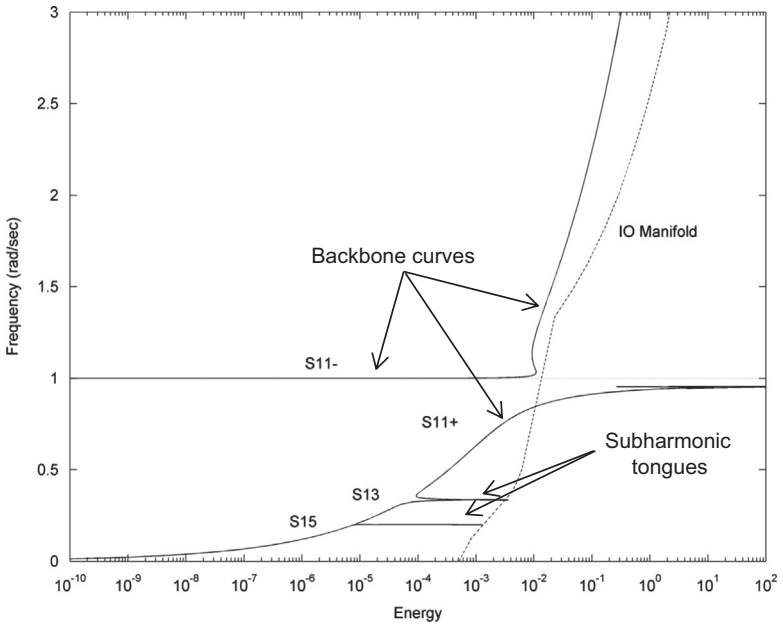

Fig. 2. Typical frequency–energy plot of the underlying Hamiltonian system (6).

system and the harvester; subharmonic orbits with frequencies below the normalized fundamental frequency of unity (such as the ones shown in Fig. 2) correspond to *slower* oscillations of the harvester with respect to the primary system, whereas subharmonic orbits with frequencies above unity (not presented in the FEP of Fig. 2) correspond to *faster* oscillations of the harvester with respect to the primary system. A countable infinity of subharmonic orbits can be realized in the Hamiltonian system, occurring in in-phase/out-of-phase pairs [22].

The third class of orbits in the FEP is composed of orbits on the *IOM* (cf. Fig. 2). There are a countable infinity of periodic and an uncountable infinity of quasi-periodic impulsive orbits of the Hamiltonian system corresponding to initial impulsive excitation of the primary system with all other initial conditions being equal to zero; i.e., $\dot{x}(0+)=I_0,\ \dot{u}(0+)=-I_0,\ x(0+)=u(0+)=0$. As shown in [19,22] orbits of the weakly non-conservative system in the neighborhood of the IOM result in strong energy transfers from the primary system to the strongly nonlinear attachment, so it is expected that these will be beneficial towards the goal of effective energy harvesting. As shown in [24], dynamic instabilities arise at bifurcation points along damped transitions in the neighborhood of the high-frequency part of the IOM, causing 'transient bursts' (instabilities) in the response of the harvester resembling self-excited resonances [25,26]. As shown in the next section, it is through the excitation of high-frequency subharmonic tongues close to the high-frequency portion of the IOM that leads to effective, strong energy harvesting. This discussion highlights the importance of the Hamiltonian FEP in our nonlinear energy harvesting approach.

In the next section we will study damped transitions in the neighborhood of the high-frequency section of the Hamiltonian FEP of (6) under single and repetitive impulsive excitation of the primary system, and show that these high-frequency transitions can lead to effective energy harvesting through sustained dynamic instabilities of the harvester response. We will perform this task by performing numerical simulations of Eq. (6) under single and repetitive impulse excitations, and then studying the resulting frequency transitions by wavelet analysis and superposition of wavelet spectra on the Hamiltonian FEP. Because the single impulse input scenario will be the basis for optimizing the electromechanical properties of (6) for effective energy harvesting, we will study it first, before considering repetitive impulsive inputs.

4. Energy harvesting under single impulse excitation

We initiate our computational study of the damped dynamics of the normalized system (6) by considering a single impulse input to the LO and studying the resulting damped transitions by performing wavelet analysis and superimposing the derived wavelet spectra on the Hamiltonian FEP; as discussed in earlier works [22,24], this type of wavelet superposition, although purely phenomenological, can provide a valuable interpretation of the nonlinear transitions as the damped nonlinear response 'tracks' different branches of the underlying Hamiltonian system. The numerical simulations presented in this section are carried out for fixed system parameters $\mu=0.1,\ \lambda=0.01,\ \zeta=0.001,\ \sigma=0$. As discussed in the previous section, weak damping should be considered in the mechanical system to ensure that the desired high-frequency damped transitions can be obtained when the electromechanical and circuit parameters, $\beta,\ \rho$, respectively, are incorporated into the system. As in [8–10], proper tuning of the circuit parameters is desired to optimize energy harvesting efficiency.

The energy harvesting efficiency measure (11) was considered to obtain an optimal set of harvester parameters β,ρ in this case. This was performed numerically by defining appropriate parameter ranges, $\beta=[0.01-1.0]$ with step $\Delta\beta=0.01$, and $\rho=[0.01-2.0]$ with step $\Delta\rho=0.01$. For each specific parameter pair (β,ρ) the model (6) was numerically integrated with initial conditions (7) for a given time period μ_T and for varying impulse intensity I_0. The energy harvesting efficiency measure (11) was then computed by post-processing the resulting time series, depicted in a contour plot with every combination of β and ρ in the aforementioned parameter ranges.

In Fig. 3 we depict contour plots of the normalized harvested energy measure $M(\tau,\mu_T;I_0)$ as a function of the system parameters ρ and β for a fixed simulation period equal to $\mu_T=47.7$ normalized time units and varying impulse intensity I_0. As deduced from these plots, the parameter pairs (β,ρ) corresponding to optimal harvested energy are dependent upon the excitation amplitude, or energy level, that the system experiences. This is to be expected since this nonlinear harvester design should depend strongly on the energy level of the dynamics. Indeed, a general feature of these results is that for lower impulse intensities (cf. Fig. 3a,b) the system shows weak to moderate energy harvesting capacity, as evidenced by the complete absence (Fig. 3a), or narrow band (Fig. 3b), of parameter ranges corresponding to strong energy harvesting. On the contrary, for higher impulse intensities (cf. Fig. 3c,d) we note the formation of 'plateaus' of strong energy harvesting, indicating robustness of harvesting for small parameter variations within these plateaus. We conclude that the contour plots of Fig. 3 can be utilized to examine the robustness of the nonlinear energy harvesting system.

Considering the results in more detail, the contour plot of Fig. 3a indicates that for this low impulse intensity there exist several narrow bands of parameter pairs for which the energy harvesting efficiency reaches at most 50 percent. By increasing the impulse intensity we obtain the contour plot of Fig. 3b for which we note that a narrow band of maximum efficiency of nearly 70 percent can be achieved. By further increasing the impulsive intensity we note from the plots of Fig. 3c and d that relatively broad plateaus of strong harvesting efficiency as high as 90 percent can be achieved at the respective energy levels. Clearly, the formation of such plateaus of strong energy harvesting provides an important freedom for designing the electrical parameters of the harvester, since small variations or uncertainties in these parameters do not appear to significantly reduce the harvesting capacity. An important remark, however, is that these findings depend on the normalized time parameter μ_T; i.e., on the normalized time interval of computation of the normalized harvesting measure (11). Indeed, if this parameter is small it can negatively affect the energy harvesting measure, so a study of the dependence of the normalized measure $M(\tau,\mu_T;I_0)$ on μ_T should also be undertaken.

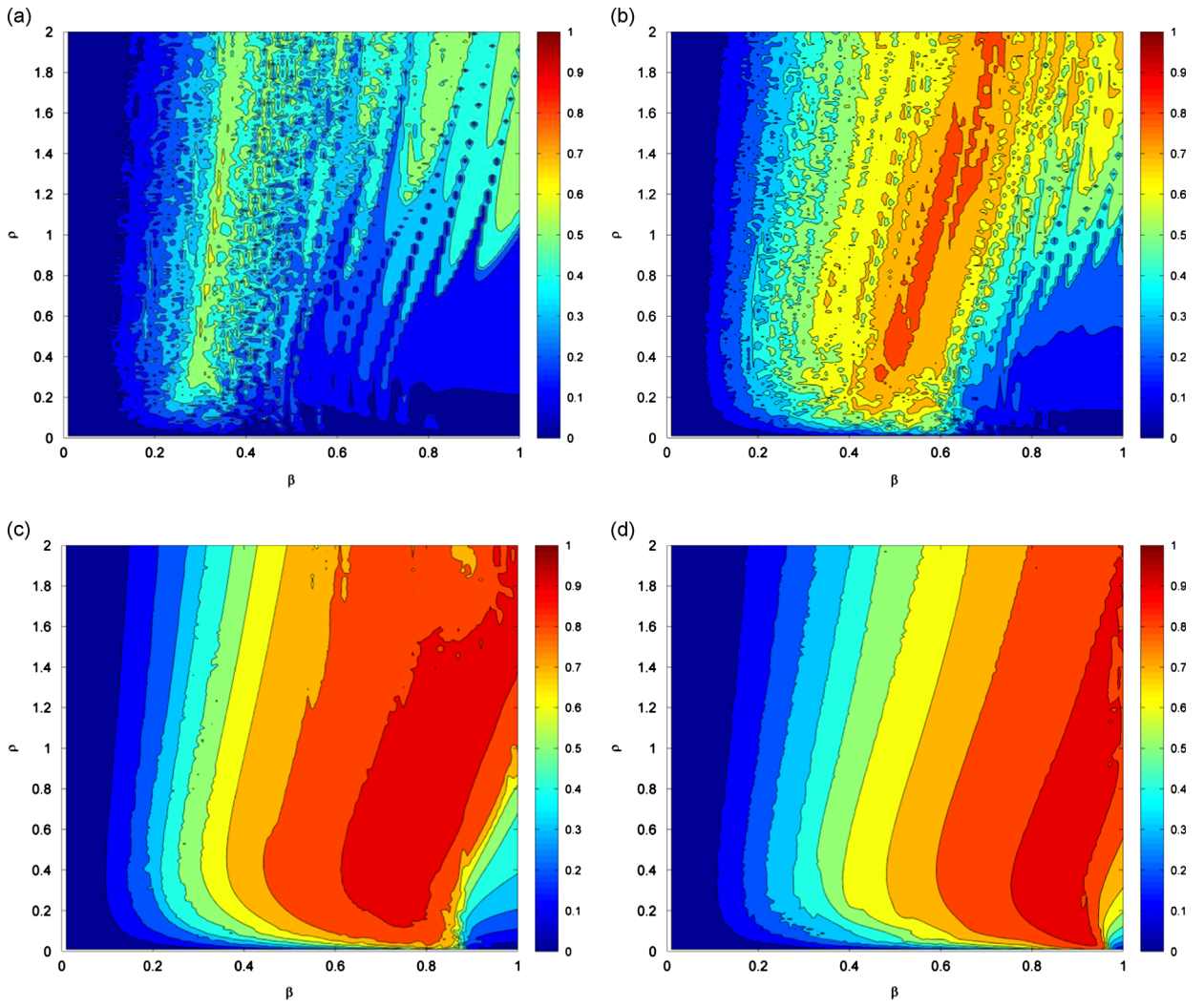

Fig. 3. Energy harvesting measure $M(\tau, 47.7; I_0)$ as a function of harvesting parameters ρ and β for normalized impulse intensity: (a) $I_0 = 0.5$, (b) $I_0 = 0.6$, (c) $I_0 = 1.0$ and (d) $I_0 = 2.0$.

We now study the dynamics governing the regimes of strong energy harvesting by relating the results of Fig. 3 to specific nonlinear dynamic transitions in the frequency–energy plot (FEP). As mentioned previously, superposition of wavelet spectra on the FEP of the underlying Hamiltonian system can provide valuable insight into the nonlinear dissipative dynamics. First, we consider the nonlinear dynamic response of the harvesting system (6) for a single impulse of normalized intensity $I_0 = 0.5$ and harvesting parameters $\beta = 0.84$ and $\rho = 1.7$. These parameters correspond to a peak in the contour plot of Fig. 3a; this, however, is one of *weak* harvesting performance of the system as described above. In Fig. 4 we depict selected transient responses of this system, together with their wavelet spectra. Considering the wavelet spectrum of the relative displacement of the harvester with respect to the primary system depicted in Fig. 4c, and its superposition on the FEP of the underlying Hamiltonian system, we note interesting resonance captures in the damped dynamics.

Initially, there is a brief 1:1 transient resonance capture (TRC) of the damped dynamics in the vicinity of the S11 − out-of-phase backbone branch of the Hamiltonian FEP, followed by escape from this TRC (due to diminishing energy) and a brief engagement in a low-frequency 1:2 TRC. Then, there is another sustained (i.e., prolonged) low-frequency 1:3 TRC, where the harvester oscillates with a frequency that is one third of the frequency of the primary system. The dynamics then remains captured in this lower frequency S13 subharmonic tongue until the remainder of the energy of the system is either harvested out of the primary system or is dissipated by viscous damping. This type of *low-frequency* damped transition resulting in low-frequency dynamical instability associated with 1:3 TRC is typical of transitions reported in purely mechanical systems of previous works [19,22], and does not lead to effective energy harvesting. Clearly, in this case the initial impulsive energy into the system is too low to allow excitations of high-frequency transient dynamic instabilities due to TRCs at high-frequency subharmonic tongues (where the harvester oscillates *faster* than the primary system). As shown below, it is precisely the excitation of such high-frequency TRCs that facilitates strong energy harvesting in system (6).

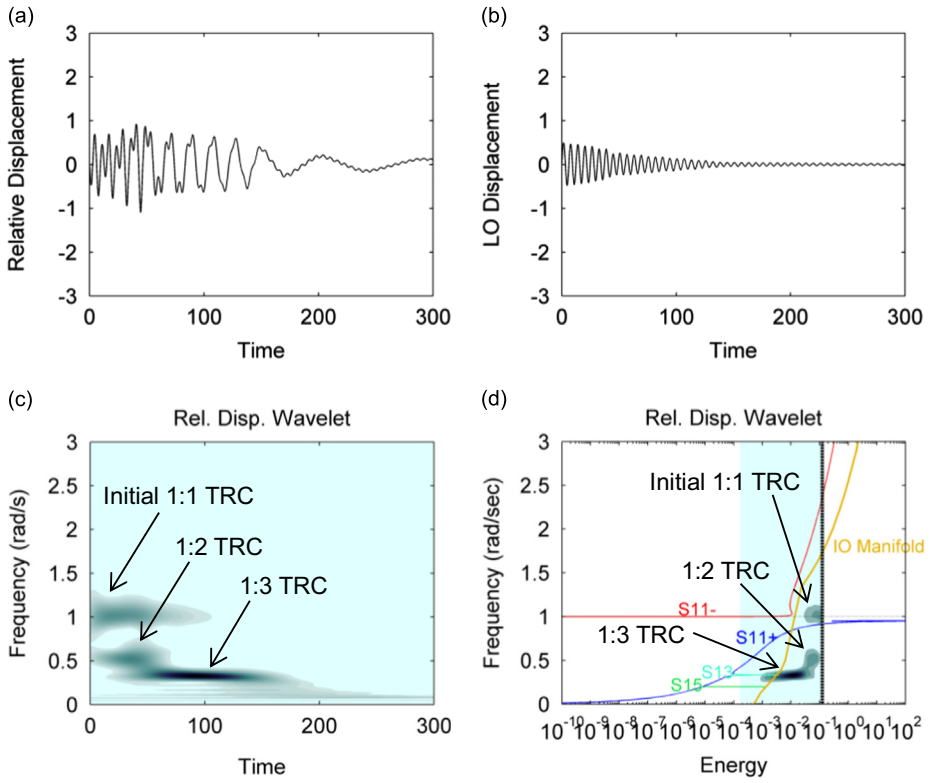

Fig. 4. Damped transient response of system (6) with $\beta = 0.84$, $\rho = 1.7$ and $I_0 = 0.5$: (a, c) time series and wavelet spectrum of relative displacement between primary system and harvester; (b) displacement of the primary system; and (d) wavelet spectrum of (a) superimposed on the FEP of the underlying Hamiltonian system.

Similar dynamics occur at the peaks of energy harvesting of the contour plot of Fig. 3b corresponding to impulse intensity $I_0 = 0.6$. At this energy level the dynamics exhibits more prolonged 1:1 TRC on the S11− backbone before transitioning once again to a S13 subharmonic TRC with decreasing energy; hence, there is a marginal enhancement of energy harvesting efficiency since this is associated with low-frequency dynamics of the harvester.

A different picture of the transient dynamics is realized; however, at the strong energy harvesting peaks of the contour plots of Fig. 3c, corresponding to higher impulse intensities. This is deduced by considering the response of system (6) for a single impulse of intensity $I_0 = 1.0$ and $\beta = 0.84$, $\rho = 1.0$, depicted in Fig. 5; these parameters correspond to the highest energy harvesting efficiency region, indicated by the plateau in Fig. 3c. Indeed, the increase in input energy results in qualitatively different transient dynamics, since now the transient response of the harvester takes place in the neighborhood of *high-frequency* subharmonic tongues in the vicinity of the upper branch portion of the IOM. This is concluded by noting the dominant high-frequency harmonics in the initial, highly energetic phase of the relative response of Fig. 5a and the corresponding wavelet spectrum of Fig. 5c. As mentioned earlier, oscillations above the normalized natural frequency of unity correspond to motions where the harvester oscillates faster than the primary system, a feature which is greatly beneficial to energy harvesting. After these initial high-frequency transients the dynamics makes a transition to the lower-frequency S11+ in-phase backbone until the remainder of the input energy is either harvested or passively dissipated. An important feature here concerns the rate at which the energy is harvested out of the primary system, which, as seen in Fig. 5b, is high, as the impulsive energy is quickly transferred to the harvester and quickly harvested by the piezoelectric element. Indeed, as seen in Fig. 5a, most of the impulsive energy input into the system is harvested within the first ~ 50 normalized time units, resulting in nearly 90 percent energy harvesting efficiency as defined by measure (11). We note that the high-frequency nonlinear instability occurring in this case is due to the high-energy TRCs realized in the initial highly energetic phase of the transient response, which, in turn, are caused by the (intentional) strong geometric nonlinearity of the harvesting system [22].

The response of the system for an impulse of intensity $I_0 = 2.0$ and for β and ρ in the highest efficiency region (plateau) of Fig. 3d exhibits similar high-frequency instabilities and transitions. This indicates that strong energy harvesting of the system of Fig. 1 is associated with excitation of high-frequency and high-energy dynamic instabilities in the lightweight harvesting element, caused by high-frequency TRCs in subharmonic tongues in the vicinity of the upper portion of the IOM of the underlying Hamiltonian system. As such, this result is similar to that reported in [24], for a purely mechanical system of strongly nonlinear coupled oscillators. Based on the results reported in this section, we conclude that strong energy harvesting under a single impulse excitation leads to rapid decay to the trivial equilibrium state of the directly excited

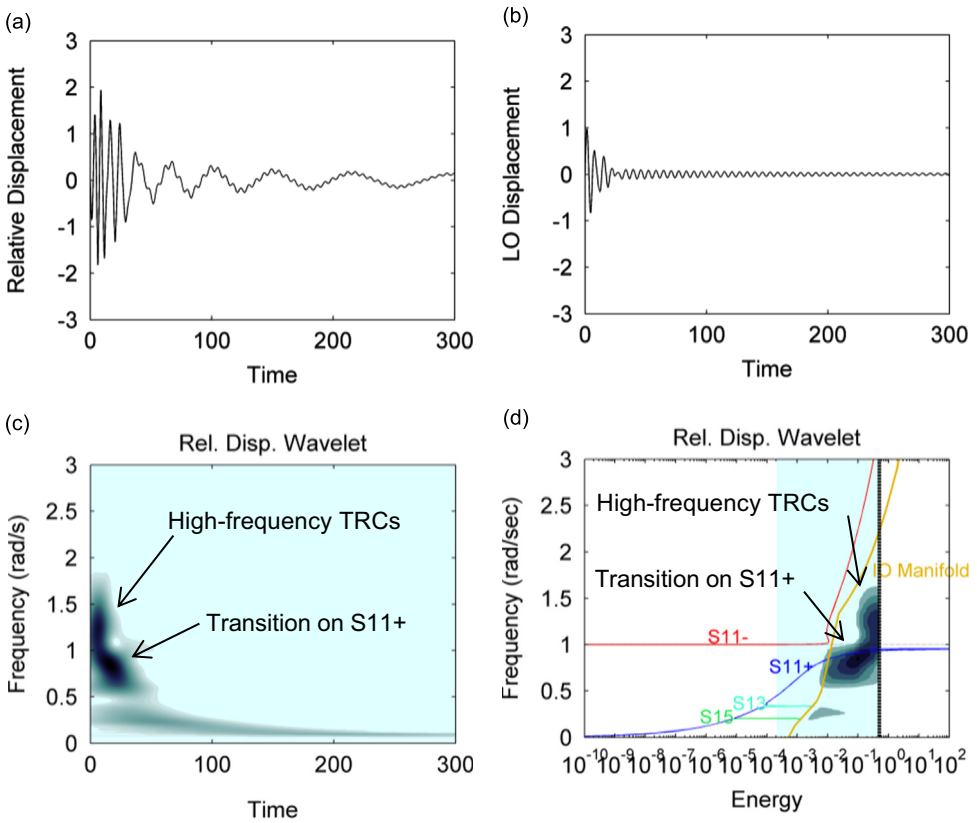

Fig. 5. Damped transient response of system (6) with $\beta = 0.84$, $\rho = 1.0$ and $I_0 = 1.0$: (a, c) time series and wavelet spectrum of relative displacement between primary system and harvester; (b) displacement of the primary system; and (d) wavelet spectrum of (a) superimposed on the FEP of the underlying Hamiltonian system.

primary system, a result that has interesting implications when one considers the extension of this study to the case of repeated impulses. Indeed, based on the previous results one can surmise that an energy harvesting system can be appropriately designed so that between impulses, the primary system returns to trivial equilibrium; in that case the strong energy harvesting efficiency (the plateaus) observed in Fig. 3c, d should be maintained under repetitive, time-periodic impulses as well. This issue is explored in detail in the next section.

5. Energy harvesting under time-periodic impulse excitation

We now consider energy harvesting in system (6) under a time-periodic pulse train (i.e., the second excitation scenario). Based on the results of the previous section, the highest energy harvesting efficiency achieved in this system under single impulse excitation was for system parameters $\mu = 0.1$, $\lambda = 0.01$, $\zeta = 0.001$, $\sigma = 0$, $\kappa = 1.0$, and impulse intensity $I_0 = 1.0$ (corresponding to the contour plots of Fig. 3c); accordingly, we select these system parameters for our study. In addition, we select electrical parameters of the harvester as $\beta = 0.84$ and $\rho = 1.0$ since these correspond to the point of optimal energy harvesting efficiency at the plateau of Fig. 3c; the resulting response of the system under single impulse excitation is then depicted in Fig. 5. Finally, the imposed initial conditions after each impulse are given by (8) with the pulse inter-arrival time μ_T and pulse intensity I_0 assumed to be fixed and considered as parameters of the problem. Our aim will be to examine the energy harvesting efficiency of the system (6) (in terms of the harvesting measures developed previously) for different values of μ_T and I_0.

Before considering the strongly nonlinear harvesting system (6), however, it will be instructive to first examine a simplified single-degree-of-freedom (sdof) linear damped oscillator excited by a periodic train of repeated impulses. The simple form of this system will allow us to derive analytical expressions for the energy harvesting measures which will be used later to interpret the direct numerical simulations of the nonlinear system (6). Following this preliminary digression we will proceed to direct numerical simulations of the considered electromechanical system using the optimized system parameters derived from the single impulse excitation (as described above). We will examine the dynamics in the temporal, energy–frequency, and time–frequency domains, and attempt an interpretation of the resulting nonlinear dynamics in terms of the analytical results derived for the linear system studied in our preliminary digression.

To this end, we consider the linear sdof damped oscillator under a periodic impulse excitation, given by

$$\ddot{x}+2\zeta\omega\dot{x}+\omega^2 x = I_0\sum_{i=0,1,2,\ldots}\delta(t-i\mu_T), \quad x(0-)=\dot{x}(0-)=0 \tag{15}$$

where ζ and ω are the critical viscous damping ratio and natural frequency, respectively. We note that the 'viscous damper' in (15) denotes the effective dissipation introduced in the linear dynamics of the primary system due to energy harvested by the harvesting element. Hence, the dissipative element in the simplified system (15) can be construed as an 'effective viscous damper' modeling the energy harvesting process. In addition we assume that (15) is a weakly underdamped system ($\zeta \ll 1$), so that the time scale of the amplitude decay of (15) is larger than the natural period of the system, $T=2\pi/\omega$, and a slow–fast partition of the damped dynamics is realized. This is a reasonable assumption for the considered problem, based on the results for the single impulse excitation analysis of the previous section (i.e., we do not anticipate the slow–fast partition of the dynamics of the primary system to be violated in this second excitation scenario).

Our analysis will be based on simple energy balance arguments, and the fact that between applied impulses the system performs free oscillations. Based on the underdamped assumption these free oscillations after the application of the ith impulse can be expressed as

$$x=\sqrt{E_i^+}\,e^{-\zeta\omega t}\,\sin\left(\sqrt{1-\zeta^2}\omega t+\delta\varphi_i\right), \quad \dot{x}\approx\left(\omega\sqrt{E_i^+}\,e^{-\zeta\omega t}\right)\cos\left(\sqrt{1-\zeta^2}\omega t+\delta\varphi_i\right) \tag{16}$$

where we denote by E_i^+ the total energy of the system immediately after the application of the ith impulse, and by $\delta\varphi_i$ the resulting phase change. From the above it is straightforward to conclude that just before the application of the next impulse the total energy of the system is

$$E_{i+1}^- = E_i^+ e^{-2\zeta\omega\mu_T} \tag{17}$$

Note that in this idealized linear framework the energy harvested after the ith impulse (defined as the energy dissipated by the 'effective viscous damper' of the oscillator) is expressed as

$$E_H = E_i^+(1-e^{-2\zeta\omega\mu_T}) \tag{18}$$

Moreover, immediately after the application of the $(i+1)$th impulse it holds that

$$\begin{aligned} x_{i+1}^+ &= \left(\sqrt{E_{i+1}^-}/\omega\right)\sin\left[\sqrt{1-\zeta^2}\omega(i+1)\mu_T+\delta\varphi_i\right] \\ \dot{x}_{i+1}^+ &\approx \sqrt{E_{i+1}^-}\,\cos\left[\sqrt{1-\zeta^2}\omega(i+1)\mu_T+\delta\varphi_i\right]+I_0 \end{aligned} \tag{19}$$

Therefore, we can express the total energy of the system immediately after the application of the $(i+1)$th impulse as

$$E_{i+1}^+ = (E_{i+1}^-/2)\left\{\sin^2\left(\sqrt{1-\zeta^2}\omega(i+1)\mu_T+\delta\varphi_i\right)+\left[\cos\left(\left(\sqrt{1-\zeta^2}\omega(i+1)\mu_T+\delta\varphi_i\right)+\left(I_0/\sqrt{E_{i+1}^-}\right)\right)\right]^2\right\} \tag{20}$$

Due to the complexity of the above equation we will proceed by restricting our study to specific values of the inter-arrival times $\mu_T = n\pi/\sqrt{1-\zeta^2}\omega$, $n=1,2,\ldots$, in which case (20) takes the form

$$E_{i+1}^+ = \frac{E_{i+1}^-}{2}\left\{\sin^2(\delta\varphi_i)+\left[\cos(n\pi+\delta\varphi_i)+\frac{I_0}{\sqrt{E_{i+1}^-}}\right]^2\right\}, \quad \mu_T = n\pi\Big/\sqrt{1-\zeta^2}\omega, \quad n=1,2,\ldots \tag{21}$$

where $\delta\varphi_i$ denotes the phase difference between the applied impulse and the harvester response. Moreover, we will further restrict our analysis to the case where either the impulse intensity satisfies the condition $I_0 \gg \sqrt{E_{i+1}^-}$, in which case the energy immediately after the impulse E_{i+1}^+ is almost purely kinetic, so $\delta\varphi_i \approx \pi$; or to the condition $I_0 \ll \sqrt{E_{i+1}^-}$, in which case the phase difference $\delta\varphi_i$ is negligible, $\delta\varphi_i \approx 0$. In both cases the following approximation holds:

$$E_{i+1}^+ \approx \frac{E_{i+1}^-}{2}\left[(-1)^n+\frac{I_0}{\sqrt{E_{i+1}^-}}\right]^2, \quad \mu_T = n\pi\Big/\sqrt{1-\zeta^2}\omega, \quad n=1,2,\ldots, \quad I_0 \gg \sqrt{E_{i+1}^-} \text{ or } I_0 \ll \sqrt{E_{i+1}^-} \tag{22}$$

Combining this equation with (17) we finally obtain

$$E_{i+1}^+ \approx \frac{1}{2}\left[(-1)^n e^{-(\zeta/\sqrt{1-\zeta^2})n\pi}\sqrt{E_i^+}+I_0\right]^2,$$

$$\mu_T = n\pi\Big/\sqrt{1-\zeta^2}\omega, \quad n=1,2,\ldots, \quad I_0 \gg \sqrt{E_{i+1}^-} \text{ or } I_0 \ll \sqrt{E_{i+1}^-} \tag{23}$$

Relation (23) defines a one-dimensional nonlinear map, and assuming that it has a stable period-1 fixed point (corresponding to stable steady-state energy harvesting), this can be computed as

$$E^+ \approx \frac{1}{2}\left[(-1)^n e^{-(\zeta/\sqrt{1-\zeta^2})n\pi}\sqrt{E^+}+I_0\right]^2, \quad \mu_T = n\pi\Big/\sqrt{1-\zeta^2}\omega, \quad n=1,2,\ldots \text{ (Steady state)} \tag{24}$$

where E^+ denotes the total energy of the system at steady state, immediately after the application of an impulse. Solving the above algebraic equation for E^+ we obtain two solutions, of which only one is physically meaningful

$$\sqrt{E^+} \approx \frac{\sqrt{2}+(-1)^n e^{-(\zeta/\sqrt{1-\zeta^2})n\pi}}{2-e^{-(2\zeta/\sqrt{1-\zeta^2})n\pi}} I_0, \quad \mu_T = n\pi\Big/\sqrt{1-\zeta^2}\omega, \quad n=1,2,\ldots \text{ (Steady state)} \tag{25}$$

Based on this analytical approximation the energy harvested per impulse at steady state can be estimated through Eq. (15) to be

$$E_H \approx I_0^2\left[\frac{\sqrt{2}+(-1)^n a^n}{2-a^{2n}}\right]^2 (1-a^{2n}), \quad \mu_T = n\pi\Big/\sqrt{1-\zeta^2}\omega, \quad n=1,2,\ldots \text{ (Steady state)} \tag{26}$$

where $a \equiv e^{-(\zeta/\sqrt{1-\zeta^2})n\pi} < 1$.

In Fig. 6 we depict the previous analytical approximation of the total energy of the system after the application of an impulse of intensity $I_0 = 1.0$ (without any loss of generality) as a function of increasing inter-arrival time μ_T for $n = 1, 2, \ldots$. We observe that for sufficiently large inter-arrival times μ_T, i.e., for sufficiently large n, the total energy of the system before the impulse reaches approximately a zero level. This agrees with physical intuition, since if the inter-arrival time between impulses is sufficiently large, there is adequate time to harvest nearly all of the available mechanical energy, so an instant before the next impulse is applied the total energy of the system is nearly zero. This is a very robust regime of energy harvesting, and it clearly represents a state of the dynamics where no differentiation of the state of the system between applied impulses exists.

For smaller inter-arrival times, however, we observe a highly oscillatory pattern between even and odd values of n. This is the case where the system continues to carry residual (unharvested) energy at the time instant of application of the next impulse. Moreover, the highly oscillatory behavior of the total energy for smaller values of n is a direct consequence of the fact that the discrete values of inter-arrival time were chosen so that the impulse was either in-phase or out-of-phase with respect to the response of the harvester. This highlights the extreme sensitivity of the energy harvesting to the relative phase of the oscillation between the harvester and the applied impulse in the regime of short to moderate inter-arrival times μ_T. Indeed, when n is even (in-phase case) we have the phenomenon of *discrete-resonance* where the impulsive energy is applied at the precise instant when the harvester can import all of it, or equivalently, this is the case where the work produced by the external impulse is maximum. On the other hand when n is odd the velocity of the mass and the applied impulse are completely out-of-phase, so the energy imported to the system is minimal. These two cases form the two extremes that bound the performance of the energy harvester. For inter-arrival times in between the considered discrete values (i.e., when n is small and non-integer) the dynamics is more complex and another approach based on stochastic analysis, is required, in order to relate the energy harvesting capacity of the system to the relative phase between the applied impulse and the harvester response. These results, along with the analysis of the energy harvesting optimization and robustness to small uncertainties in either the inter-arrival times or the impulse intensities, will be considered in detail in a future work. This ends the digression with the linear harvester (15), which highlighted some simple but important aspects related to the dynamics of energy harvesting under impulse excitation. This dynamics is expected to apply to the case of the nonlinear harvester (12) which we now proceed to examine.

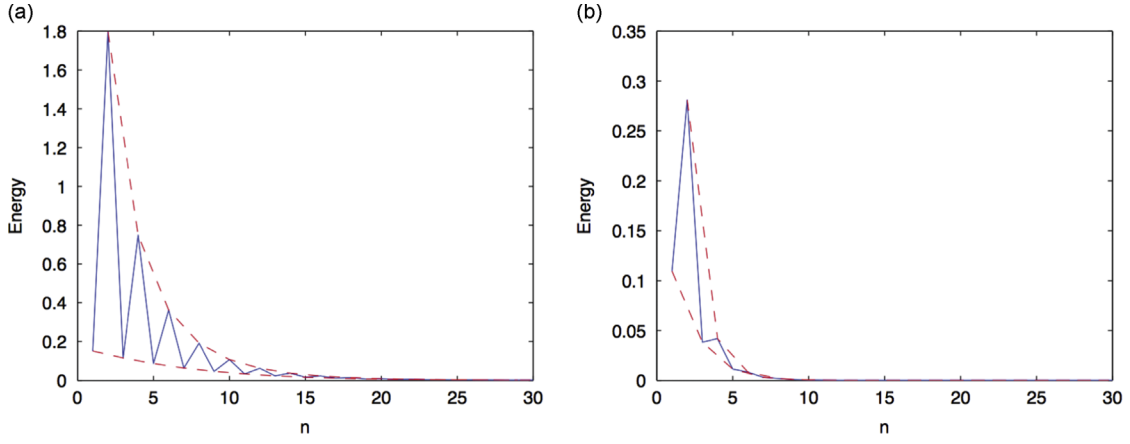

Fig. 6. Analytical approximation of the total energy before the application of the impulse at steady state for system (12) for $I_0 = 1.0$: (a) $a = 0.7$ and (b) $a = 0.9$.

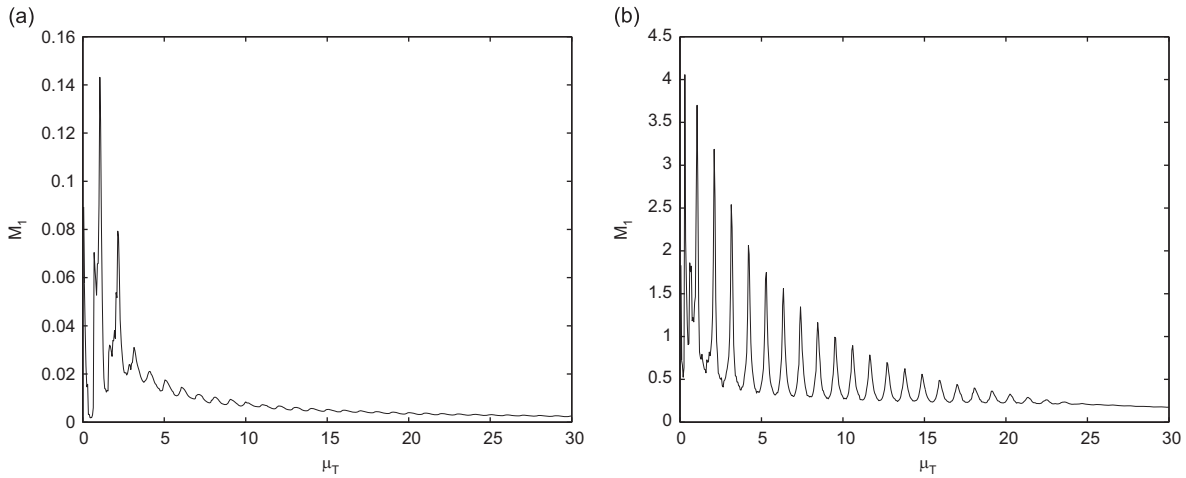

Fig. 7. Time-averaged harvested energy M_1 for the nonlinear harvesting system (6) as a function of inter-arrival time μ_T for impulse intensity: (a) $I_0 = 1.0$ and (b) $I_0 = 10.0$.

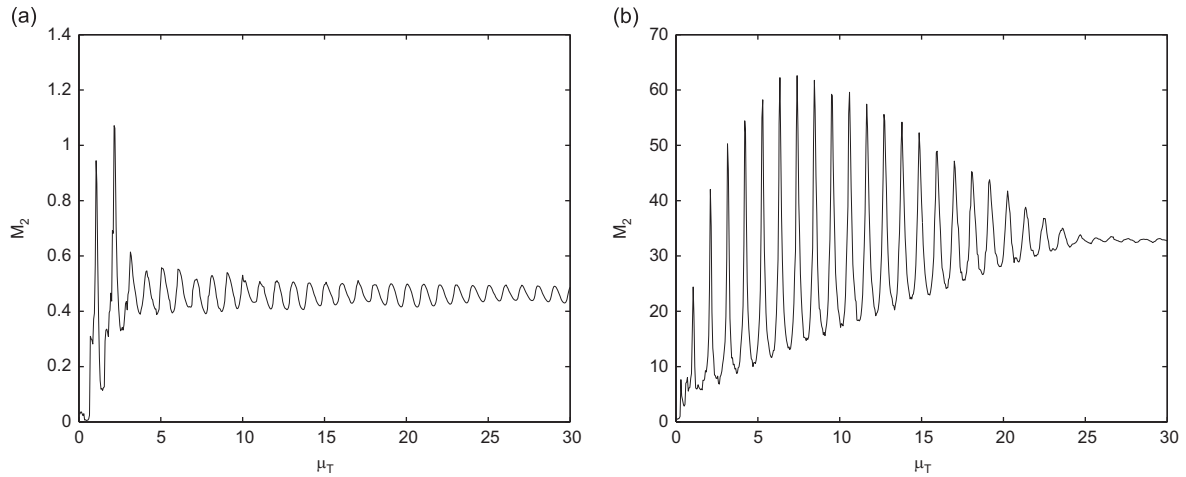

Fig. 8. Impulse-averaged harvested energy M_2 for the nonlinear harvesting system (6) as a function of inter-arrival time μ_T for impulse intensity: (a) $I_0 = 1.0$ and (b) $I_0 = 10.0$.

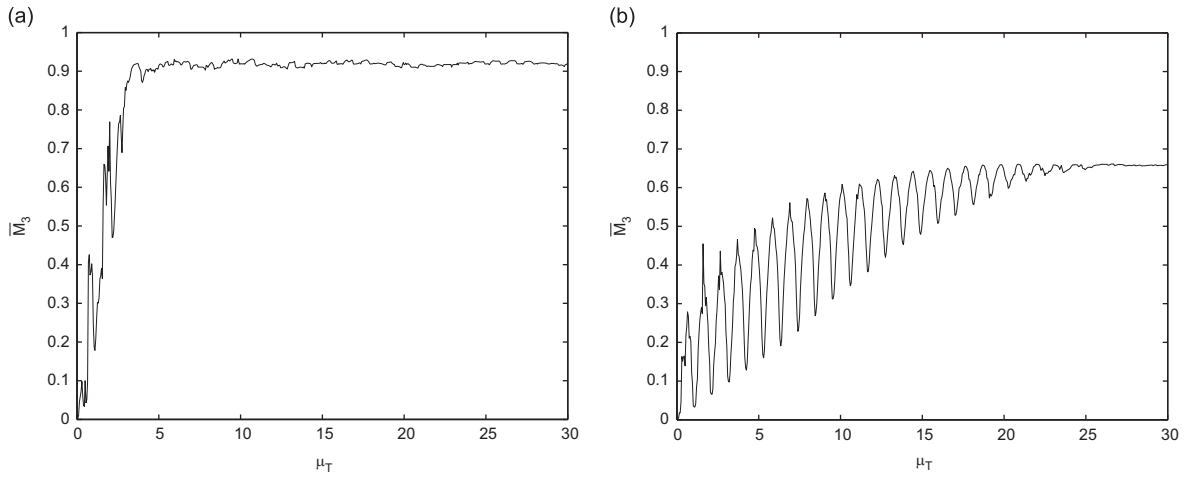

Fig. 9. Impulse-averaged canonical harvested energy measure $\overline{M_3}$ for the nonlinear harvesting system (6) as a function of inter-arrival time μ_T for impulse intensity: (a) $I_0 = 1.0$ and (b) $I_0 = 10.0$.

The parameters for the system were selected based on the optimal values derived for the single impulse excitation as discussed in the beginning of this section. First, we examine the energy harvesting measures (12)–(14) defined in Section 2 for this specific system. In Figs. 7–9 we depict the measures M_1, M_2 and $\overline{M_3}$ as functions of the inter-arrival time μ_T for two different impulse intensities; these results were derived by direct numerical simulations of Eq. (6) with initial conditions (8). We note that consistent with the linear analysis presented previously, there exists a 'phase-dependent' regime of the dynamics realized for sufficiently small inter-arrival times, where depending on the relative phase between the primary system and the applied impulse maximal or minimal absorption ('pumping') of energy in the harvesting system can be realized. Clearly, this feature is independent of the nonlinear nature of the harvester and can be predicted using simple power absorption arguments similar to the ones used in the digression above.

However, as the inter-arrival time decreases fluctuations in the energy harvesting performance gradually decrease to where they are completely eliminated. Hence, there exists a critical value of the inter-arrival time μ_T above which the entire mechanical energy in the primary system following the application of an impulse is nearly dissipated or harvested before the next impulse is applied, similar to the linear harvester discussed in the digression. In that case the impulse-averaged harvested energy measure M_2 reaches a constant asymptotic value which corresponds to the total energy in the system immediately after the application of each impulse after subtracting the energy dissipated per cycle due to viscous damping. In addition, for longer inter-arrival times the efficiency of the energy harvesting gradually decreases (e.g., consider measure M_1), since the impulses arrive infrequently and the primary system nearly reaches the trivial equilibrium between applied impulses.

Consider the third measure $\overline{M_3}$, which provides the average ratio of harvested energy normalized by the energy induced in the system (and hence, available for harvesting) immediately after the application of each impulse. It turns out that this 'utility' average measure reaches its maximum value when the inter-arrival time is sufficiently large so that most of the system energy has been dissipated before the next impulse is applied. This result combined with the conclusions made from measure M_1 defines as a combined optimum (for all three energy harvesting measures) an inter-arrival time that is

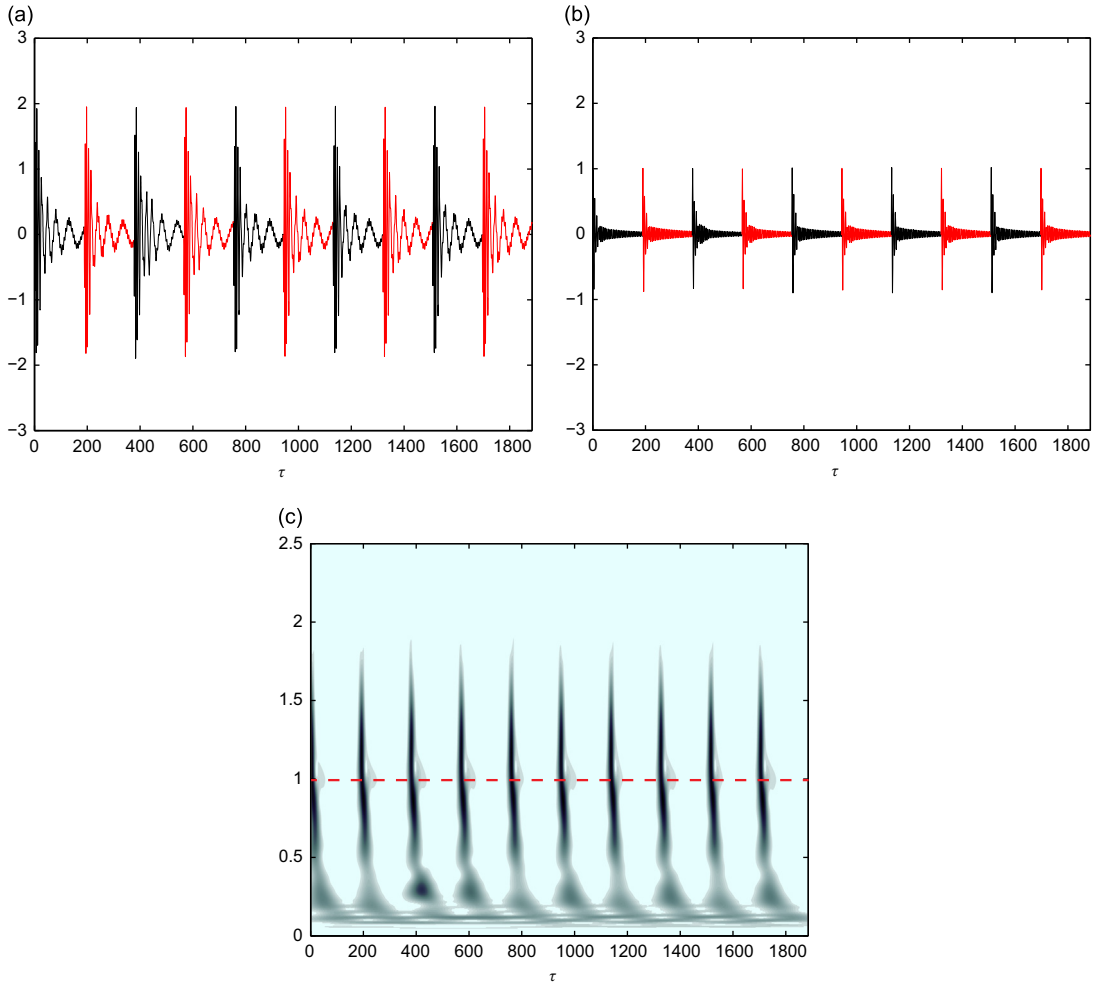

Fig. 10. Case of efficient nonlinear energy harvesting for $I_0 = 1.0$ and $\mu_T = 30$: (a) relative response between primary system and harvester; (b) response of the primary system; and (c) wavelet spectrum of (a). The dashed line indicates the normalized natural frequency of the primary system.

comparable with the time required for the system to almost completely harvest or dissipate the energy it acquires after an applied impulse.

To analyze the dynamics of the harvester in more detail we select a response from the robust regime of energy harvesting for the case $I_0 = 1.0$ corresponding to inter-arrival time $\mu_T = 30$. The relative response between the primary system and the harvester is depicted in Fig. 10a, the response of the impulsively excited primary system in Fig. 10b, and the wavelet spectrum of the relative response time series in Fig. 10c. Clearly, we deduce that during each cycle of impulsive excitation the induced energy is rapidly and effectively harvested, so by the time of application of the next impulse the system reaches the near-trivial equilibrium state. As a result, the dynamics of system (6) is nearly periodic, starting from the first cycle; i.e., no transition to the steady state of efficient energy harvesting exists and the system reaches a state of efficient harvesting immediately following the application of the first impulse at $\tau = 0+$. As noted from the wavelet spectrum of Fig. 10c the governing dynamic mechanism leading to efficient energy harvesting is a high-frequency dynamic instability in the harvester response due to the excitation of a high-frequency subharmonic TRC, as discussed in Section 4. Contrary to the single-impulse excitation, however, this series of dynamic instabilities is sustained due to the appropriate design of the electromechanical parameters of the harvesting system and the appropriate selection of the inter-arrival time μ_T.

The dynamic instability of the harvester response is further highlighted in the frequency–energy plot of Fig. 11, where the wavelet spectrum of the third cycle of the impulsive relative response of Fig. 10a is superimposed on the FEP of the underlying Hamiltonian system. We notice the high-frequency TRCs occurring in the initial highly energetic phase of the impulsive response, in the neighborhood of the high-frequency branch of the IOM, which leads to rapid targeted energy transfers from the primary system to the harvester. That this is indeed the case is confirmed by the rapid decay of the transient response of the primary system (cf. Fig. 10b) and the simultaneous high-amplitude and high-frequency oscillation (manifested as transient dynamic instability) of the nonlinear harvester. We note that similar dynamics occurs during each cycle of the relative response of Fig. 10a, justifying the high efficiency of energy harvesting in this system.

Next, we analyze the dynamic response of the harvester in the phase-dependent regime corresponding to relatively small inter-arrival times, realized for impulse intensity $I_0 = 1.0$ and inter-arrival time $\mu_T = 1.19$. In this case there is significant residual energy remaining in the system when a subsequent impulse is applied, so the non-trivial state of the system during the application of each impulse is expected to significantly influence its energy harvesting capacity. In Fig. 12 we depict the transient dynamics of the harvester in this phase-dependent case. The first distinctive difference relative to the robust case is the aperiodic character of the transient response. Moreover, we observe that in contrast to the robust regime in this case the energy of the vibration is confined mainly in the neighborhood of the natural frequency of the primary system. Although some high-frequency oscillations are realized, these are weak and the high-frequency dynamic instability that led to strong energy harvesting in the previous case is now completely missing. These conclusions are confirmed by the FEP of Fig. 13 which depicts

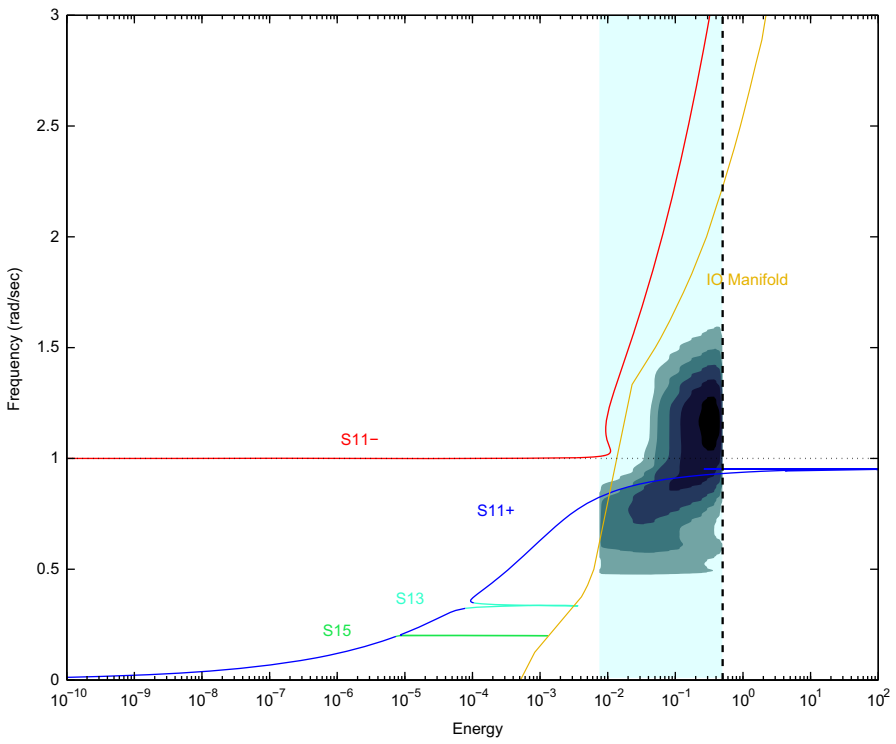

Fig. 11. Wavelet spectrum of the relative response depicted in Fig. 10a superimposed on the FEP of the underlying Hamiltonian system for the third cycle of impulsive excitation.

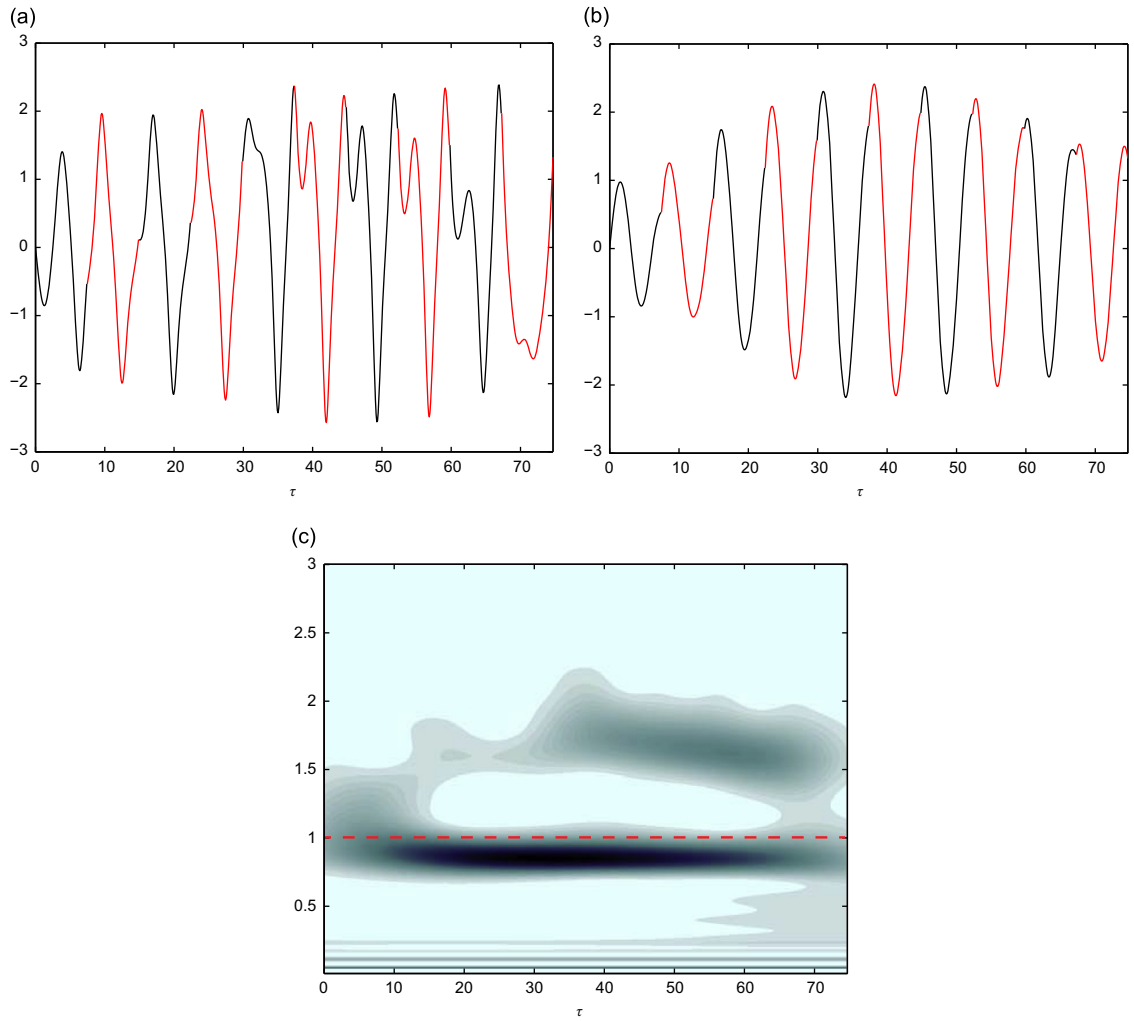

Fig. 12. Case of efficient nonlinear energy harvesting for $I_0 = 1.0$ and $\mu_T = 1.19$: (a) relative response between primary system and harvester; (b) response of the primary system; and (c) wavelet spectrum of (a). The dashed line indicates the normalized natural frequency of the primary system.

the wavelet spectrum of the relative response superimposed on the Hamiltonian FEP. As a result in this dynamic regime there is much lower utilization of the total energy after each impulse, and the energy harvesting efficiency is low as confirmed by measure $\overline{M_3}$, which is sub-optimal in this sense (cf. Fig. 9).

We emphasize, however, that even in this phase-dependent regime of energy harvesting the time-averaged energy harvested measure M_1 can attain higher values than the previous robust harvesting regime, and to this end further analysis, based on a stochastic approach is required to analyze the efficiency of energy harvesting. The previous studies revealed the sensitivity of the efficiency of energy harvesting in system (6) for fixed impulse intensity and varying inter-arrival time. We now proceed to the study of the harvesting system under periodic pulse train excitation for fixed inter-arrival times and varying impulse intensity.

The results in terms of the three harvesting measures are shown in Figs. 14–16. The first two measures show an almost monotonic increase of the energy harvested with respect to impulse intensity for small and large inter-arrival times. More information is provided by the third measure, which depicts the capacity of the system to harvest the available energy after the application of an impulse; i.e., the utilization of the available energy after each impulse. In particular, this measure shows an increasing trend for the smaller impulse intensities, which slowly decreases after reaching a maximum close to $I_0 = 1.0$. This tendency is observed for both cases of inter-arrival times considered. As discussed in Section 4, low-intensity impulses lead to damped dynamic transitions on low-frequency subharmonic tongues, which result in lower energy harvesting efficiency. However, higher-magnitude impulses (near an optimal value of unity) result in damped transitions in the neighborhood of the high-frequency IOM, which result in high energy harvesting efficiency. This explains the trends observed in Figs. 14–16.

In Fig. 17 we present a computational study of the dependences of the three energy harvesting measures on both the impulse intensity and the inter-arrival time in order to get the complete picture of the effectiveness of the electromechanical

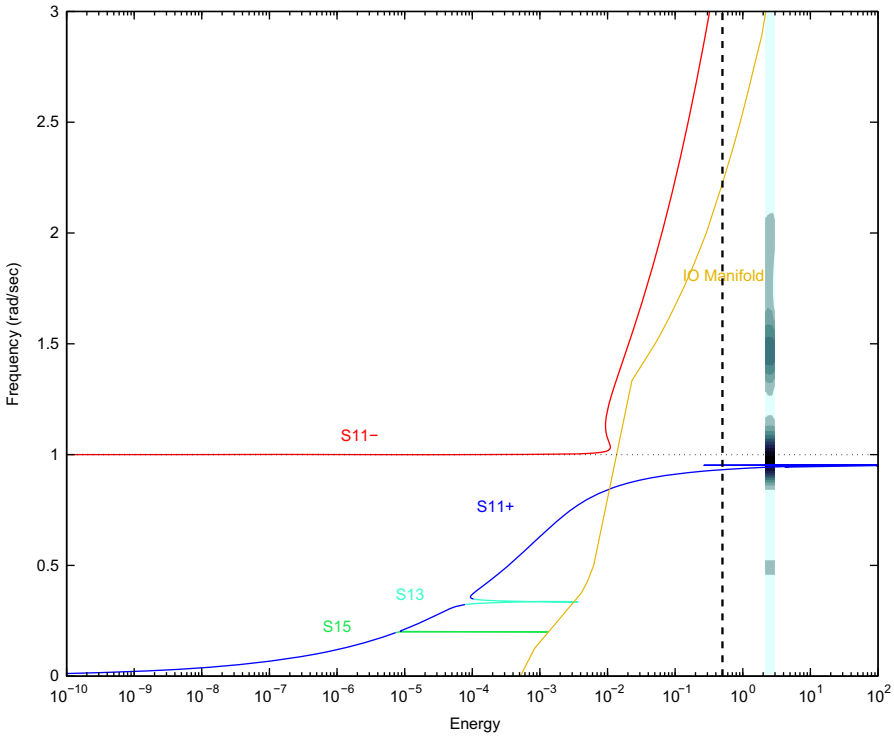

Fig. 13. Wavelet spectrum of the relative response depicted in Fig. 12a superimposed on the FEP of the underlying Hamiltonian system for the seventh cycle of impulsive excitation.

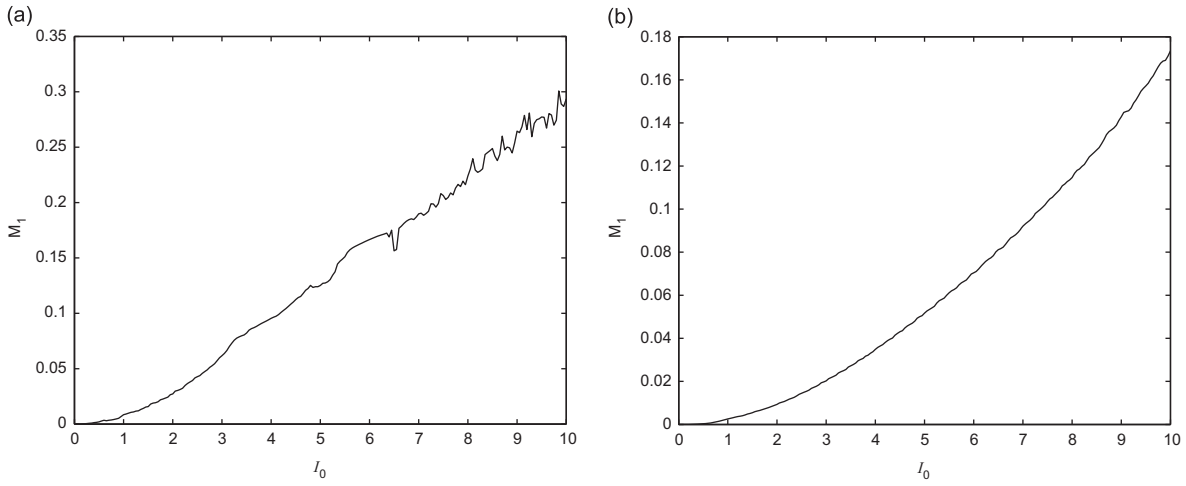

Fig. 14. Time-averaged harvested energy M_1 for the nonlinear harvesting system (6) as a function of impulse intensity I_0 for inter-arrival time (a) $\mu_T = 10$ and (b) $\mu_T = 30$.

system (6) as the parameters of the applied pulse trains vary. The previous results depicted in Figs. 14–16 thus represent 'slices' of the corresponding three-dimensional plots of Fig. 17. Considering the information provided by the harvesting measure $\overline{M_3}$ (Fig. 17c) we deduce that an efficient energy harvesting regime is realized for pulse train parameters $I_0 \approx 1$ and $\mu_T > 4$. On the other hand, the average energy harvesting measure M_1 depicted in Fig. 17a indicates that an inter-arrival time greater than $\mu_T = 5$ might be excessive, since in that case the periods between impulses are so large that the energy harvesting device returns to its trivial equilibrium state before the next impulse is applied. Hence a redundancy occurs with the device becoming under-utilized. Also, as mentioned previously, the impact-averaged measure M_2 (cf. Fig. 17b) provides us with another indication of the effectiveness of energy harvesting in this parameter regime. It follows that parametric studies such as the ones reported in Fig. 17 enable one to design system (6) for optimal energy harvesting for time-periodic pulse train excitation of given impulse intensity and inter-arrival time.

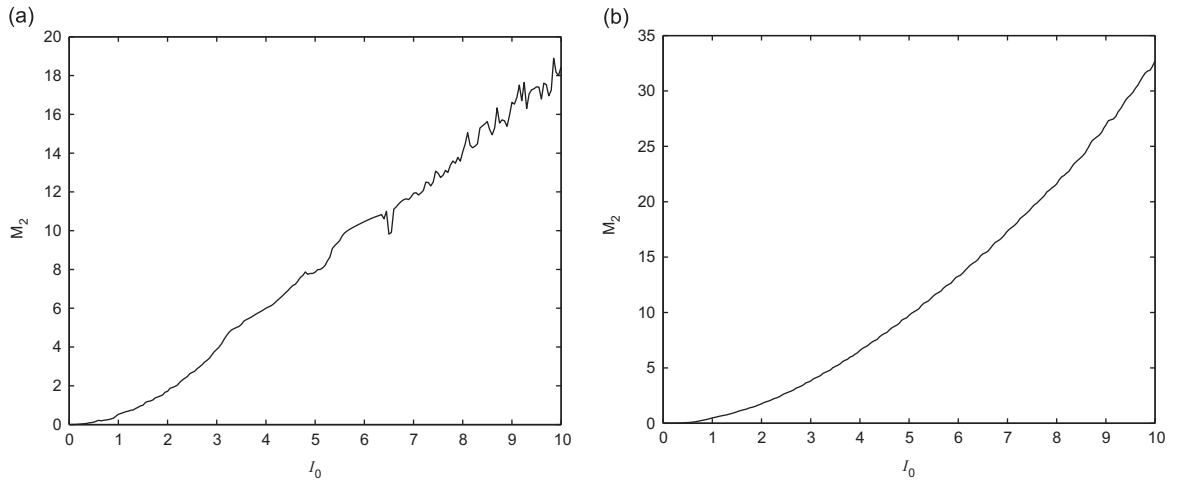

Fig. 15. Time-averaged harvested energy M_2 for the nonlinear harvesting system (6) as a function of impulse intensity I_0 for inter-arrival time: (a) $\mu_T = 10$ and (b) $\mu_T = 30$.

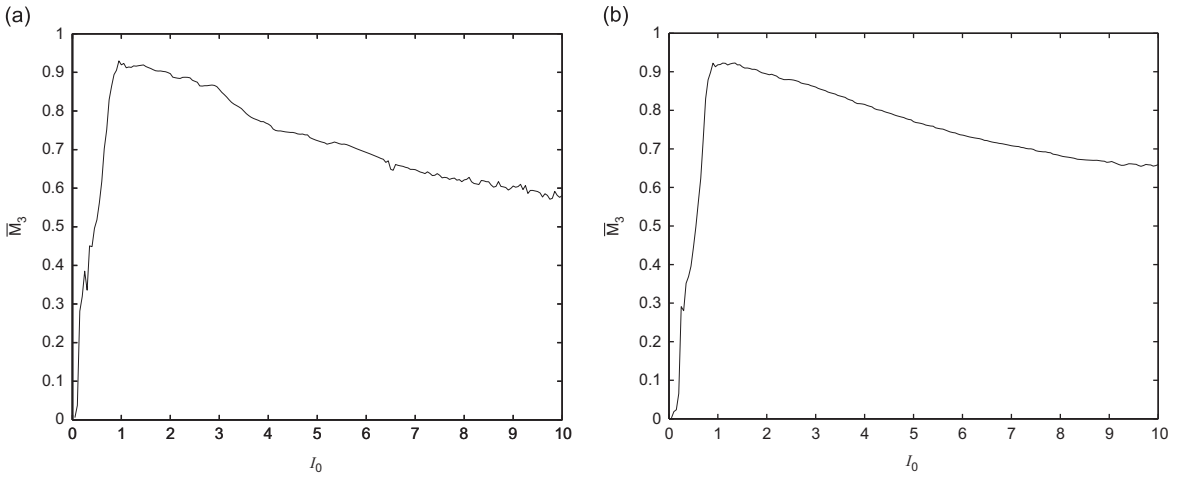

Fig. 16. Impulse-averaged canonical harvested energy measure $\overline{M_3}$ for the nonlinear harvesting system (6) as a function of impulse intensity I_0 for inter-arrival time: (a) $\mu_T = 10$ and (b) $\mu_T = 30$.

Despite the usefulness of these results, however, they do not provide any measure of robustness of energy harvesting to parameter variations in the harvester itself. To this end, it would be desirable to perform such a robustness study by extending for the case of repetitive impulses the similar study performed in Section 4 where 'plateaus' of strong energy harvesting were noted over variations of the electromechanical parameters β and ρ of the harvester (cf. Fig. 3).

Based on the previous study, for the normalized system parameters considered, we select an optimal impulse intensity of the pulse train equal to $I_0 = 1$ and consider variable inter-arrival times μ_T. The previous results were derived for electromechanical parameters of the harvester $\mu = 0.1$, $\lambda = 0.01$, $\zeta = 0.001$, $\sigma = 0$, $\kappa = 1.0$, $\beta = 0.84$ and $\rho = 1.0$, and now we wish to investigate the robustness of energy harvesting in the optimal regime by varying the parameters β and ρ (as in Section 4). In particular, we examine if 'plateaus' of highly efficient energy harvesting, indicating robustness, appear in suitably constructed contour plots, similar to Fig. 3 for the case of single impulse excitation.

To achieve this goal we will consider the dependence of the energy measure $\overline{M_3}$ (as the main indicator of energy harvesting efficiency) on the parameters β and ρ for varying μ_T, while keeping all other system parameters and the impulse intensity fixed. We will restrict our attention to the neighborhood of $(\beta, \rho) = (0.84, 1.0)$, which was considered in the previous optimization study, and examine the energy harvesting efficiency of system (6) in that neighborhood for two different inter-arrival times $\mu_T = 1$ and 5.

In Fig. 18 we depict contour plots of $\overline{M_3}$ as a function of β and ρ for the first four impulse cycles when $\mu_T = 1$. Each of these plots was constructed by evaluating the measure $\overline{M_3}$ from direct numerical simulations of Eq. (6) subject to the specific initial conditions (8) at the start of the considered impulsive cycle; alternatively, these plots reveal how the capacity of energy harvesting depends on the system parameters and the inter-arrival time, as well as the state of the harvester at the

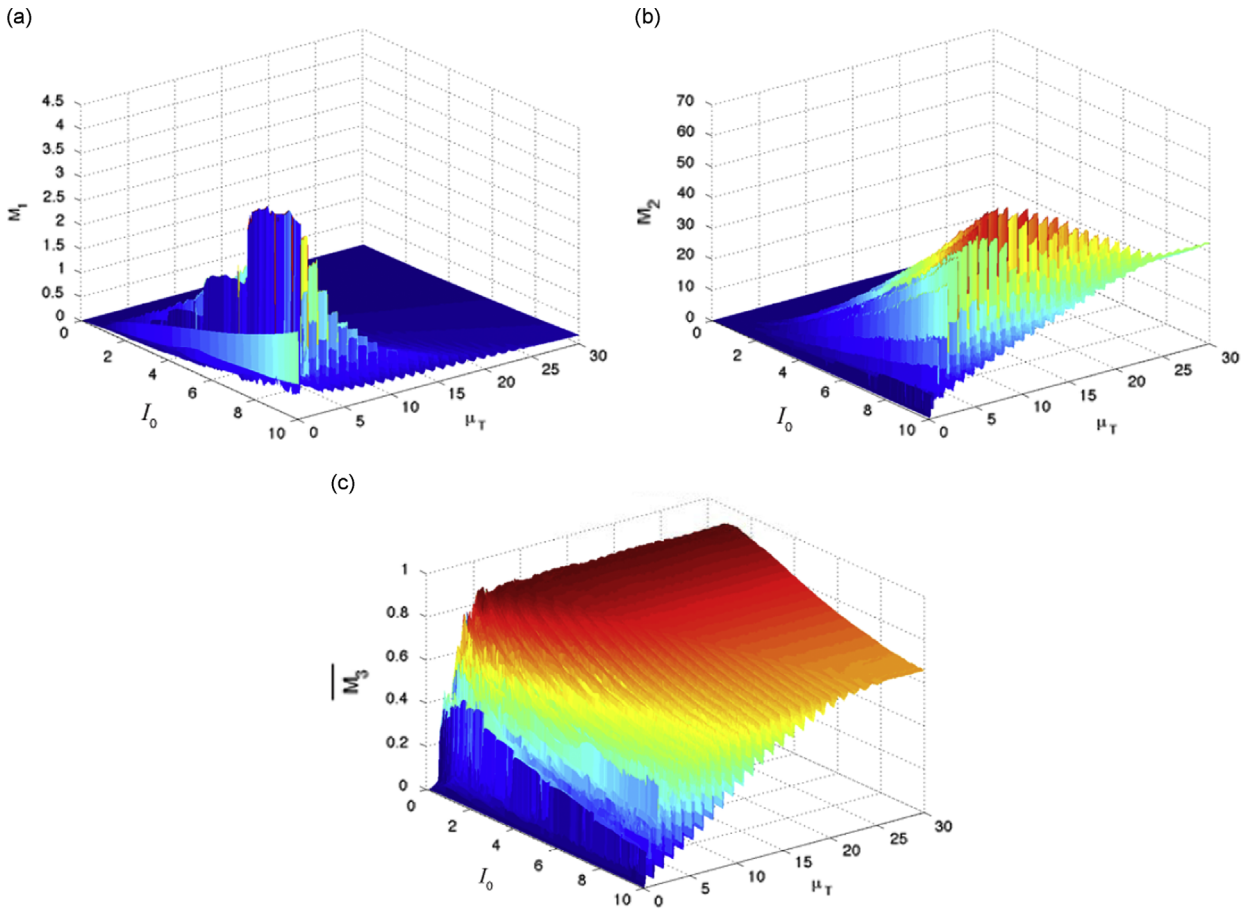

Fig. 17. Energy harvesting performance as a function of impulse intensity and inter-arrival time: (a) measure M_1, (b) measure M_2, and (c) measure $\overline{M_3}$.

beginning of each impulsive cycle. The optimal design point $(\beta,\rho)=(0.84,1.0)$ is indicated by a cross in each of these plots. As seen from Fig. 18, the contour plots change both qualitatively and quantitatively with each applied impulse; however, for this small inter-arrival time the harvesting efficiency is in general small. This is indicated by the absence of a 'plateau' of high values of the harvesting measure, a result which correlates with our previous results. In conclusion, the results indicate a consistently low level of energy harvesting irrespective of the choice of parameters β and ρ, and the process is mainly dominated by the short inter-arrival time μ_T as well as the state of the harvester at the beginning of each impulsive cycle.

In Fig. 19 we depict the corresponding contour plots for $\overline{M_3}$ for the higher inter-arrival time $\mu_T=5$, and a completely different picture of energy harvesting efficiency emerges. In this case, the larger inter-arrival time enables the dynamics to form 'plateaus' of high values of measure $\overline{M_3}$ right from the first impulsive cycle. Indeed, for each of the leading four cycles depicted, we note the formation of a plateau of strong energy harvesting in the neighborhood of the optimal point $(\beta,\rho)=(0.84,1.0)$, indicating robustness of the energy harvesting dynamics. As discussed in Section 4, on these plateaus there occur high-frequency TRCs at the beginning of each cycle, leading to high-frequency dynamic instability of the harvesting element, and, hence, to efficient energy harvesting. On the contrary, for small inter-arrival times (cf. Fig. 18), low-frequency TRCs are realized in the transient dynamics between cycles, which are not favorable to the energy harvesting objective. A final note regarding the plots of Figs. 18 and 19 is that they can be considered as extensions for the repetitive impulse case (second impulse excitation scenario) of the plot of Fig. 3, constructed for the single impulse case (first impulse excitation scenario). As such, these plots provide an integrated picture of the effects of parameter changes on energy harvesting capacity as the inter-arrival time changes. Using this methodology the robustness of the energy harvesting operation can be systematically and thoroughly studied.

6. Concluding remarks

We considered a strongly nonlinear electromechanical energy harvester excited by single or repetitive impulses. The system consists of a directly excited linear harmonic oscillator (the primary system) coupled to a lightweight attachment (the harvesting component). Although the system considered is composed of linear mechanical elements, there appear strongly nonlinear (in fact,

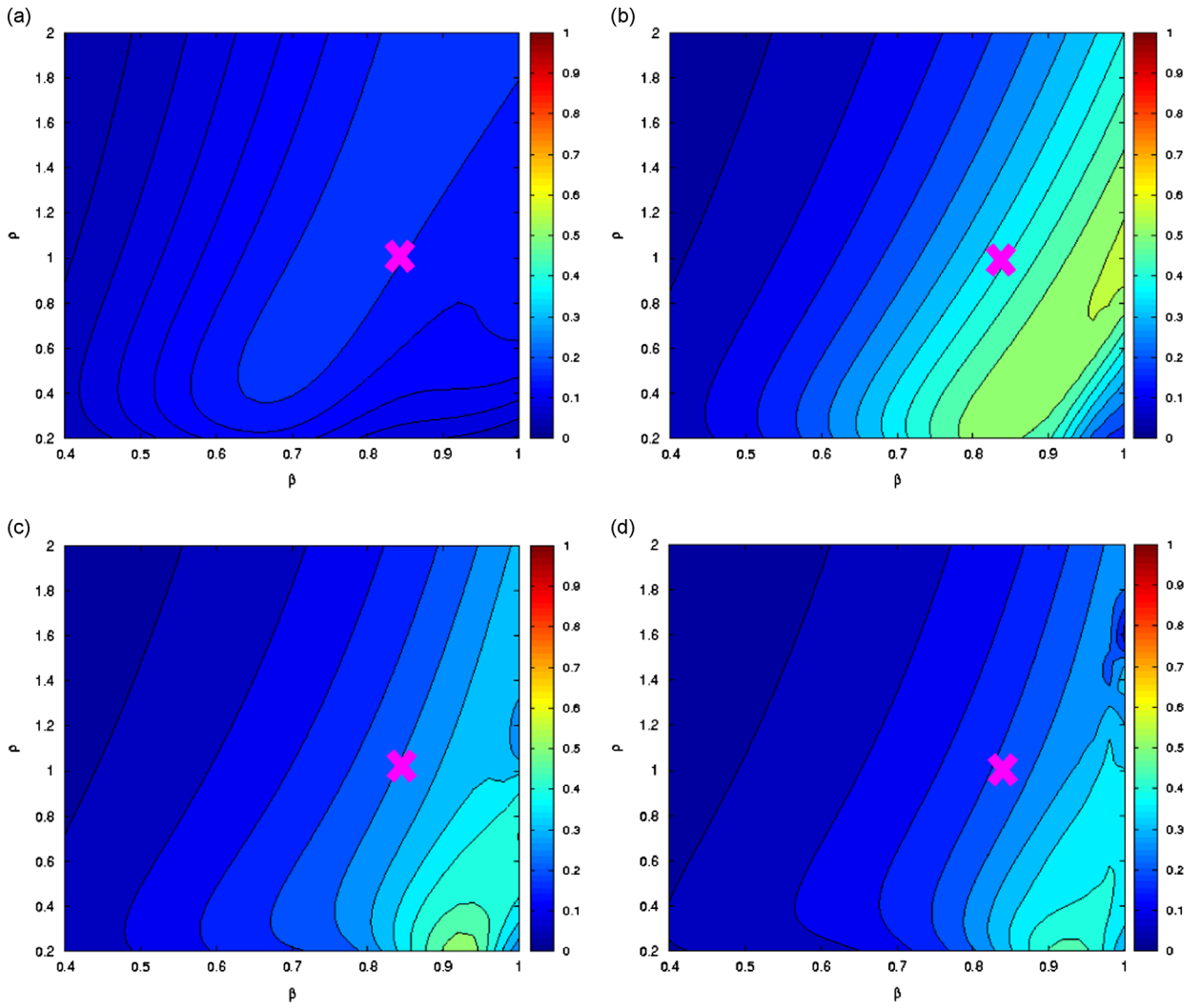

Fig. 18. Contour plots of measure $\overline{M_3}$ as a function of ρ and β for impulse intensity $I_0 = 1.0$ and inter-arrival time $\mu_T = 1$ for leading impulsive cycles: (a) cycle 1, (b) cycle 2, (c) cycle 3, and (d) cycle 4.

nonlinearizable) stiffness effects which, in turn give rise to strongly nonlinear transient resonance captures in the transient dynamics. Low-frequency TRCs are not favorable to the energy harvesting objective, since they lead to low-frequency oscillations of the lightweight harvesting element. On the contrary, high-frequency TRCs occurring in the neighborhood of the IOM of the underlying Hamiltonian system give rise to high-frequency dynamic instability of the harvesting element, which undergoes high-amplitude, high-frequency damped oscillations in the initial, highly energetic regime of the impulsive response of the system. These high-frequency instabilities result in strong energy harvesting through the realization of rapid nonlinear targeted energy transfers from the primary structure to the harvesting element.

We showed that for an appropriate harvester design this type of high-frequency dynamic instability can be sustained under repetitive impulsive excitations, resulting in sustained high-efficiency nonlinear energy harvesting. The methodologies developed in this work enable the design of the harvesting system for robust efficiency, which is confirmed by extensive computational studies presented herein. This task was achieved by developing suitable energy harvesting measures for both single and repetitive impulse excitations. In addition, low or high values of these harvesting measures were interpreted by carefully examining the wavelet spectra of the nonlinear transient dynamics of the harvester, superimposed on the frequency–energy plot of the underlying Hamiltonian system. The aforementioned low- and high-energy TRCs become evident in these depictions.

Of considerable interest would be to extend the results of this work for the case of pulse train excitations in which both the impulse intensities and the inter-arrival times between successive impulses vary stochastically. Moreover, it would be of interest to assess the efficacy of the proposed nonlinear harvesting design applied to excitations of narrower frequency

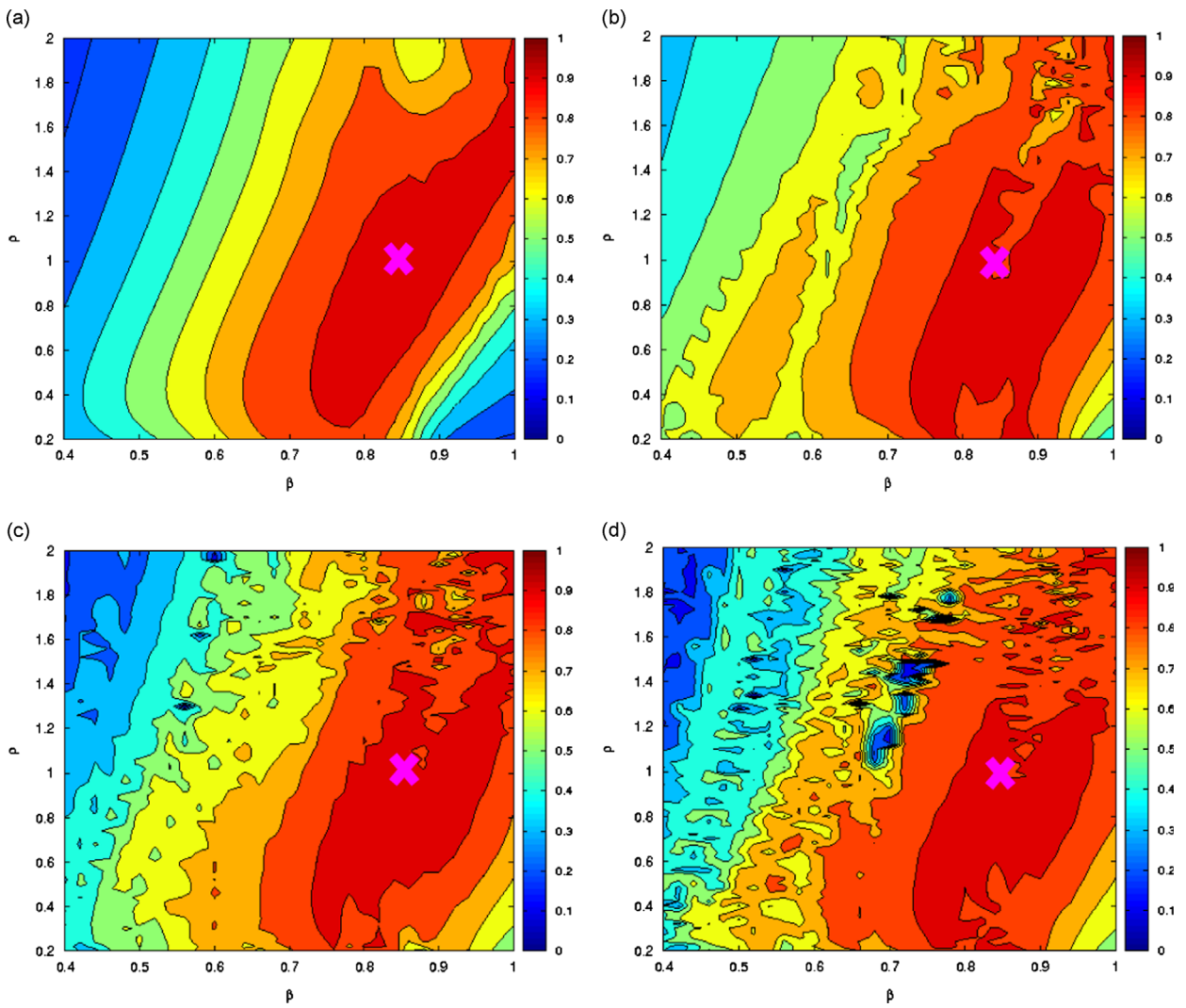

Fig. 19. Contour plots of measure $\overline{M_3}$ as a function of ρ and β for impulse intensity $I_0 = 1.0$ and inter-arrival time $\mu_T = 5$ for leading impulsive cycles: (a) cycle 1, (b) cycle 2, (c) cycle 3, and (d) cycle 4.

bands. Current efforts by the authors focus on the experimental verification of the developed theoretical design, with the results to be presented in future work.

Acknowledgments

This work was supported in part by National Science Foundation Grant CMMI-1100722. TPS and HKJ are supported by a startup grant at MIT.

References

[1] S. Roundy, P.K. Wright, A piezoelectric vibration based generator for wireless electronics, *Smart Materials and Structures* 13 (2004) 1131–1142.
[2] H.A. Sodano, D.J. Inman, G. Park, Comparison of piezoelectric energy harvesting devices for recharging batteries, *Journal of Intelligent Material Systems and Structures* 16 (2005) 799–807.
[3] S.P. Beeby, M.J. Tudor, N.M. White, Energy harvesting vibration sources for microsystems applications, *Measurement Science and Technology* 17 (2006) R175–R195, http://dx.doi.org/10.1088/0957-0233/17/12/R01.
[4] H.A. Sodano, D.J. Inman, G. Park, A review of power harvesting from vibration using piezoelectric materials, *Shock and Vibration Digest* 36 (3) (2004) 197–205.
[5] S.R. Anton, H.A. Sodano, A review of power harvesting using piezoelectric materials, *Smart Materials and Structures* 16 (2006) R1–R21.
[6] N.G. Stephen, On energy harvesting from ambient vibration, *Journal of Sound and Vibration* 293 (2006) 409–425.

[7] Y. Liao, H.A. Sodano, Model of a single mode energy harvester and properties for optimal power generation, *Smart Materials and Structures* 17 (2008) 065026.
[8] E. Lefeuvre, A. Badel, C. Richard, D. Guyomar, Piezoelectric energy harvesting device optimization by synchronous electric charge extraction, *Journal of Intelligent Material Systems and Structures* 16 (2005) 865–876.
[9] A. Badel, D. Guyomar, E. Lefeuvre, C. Richard, Efficiency enhancement of a piezoelectric energy harvesting device in pulsed operation by synchronous charge inversion, *Journal of Intelligent Material Systems and Structures* 16 (2005) 889–901.
[10] D.D. Quinn, A.L. Triplett, L.A. Bergman, A.F. Vakakis, Comparing linear and essentially nonlinear vibration-based energy harvesting, *Journal of Vibration and Acoustics* 133 (2011) 011001-1.
[11] N. duToit, B. Wardle, Experimental verification of models for microfabricated piezoelectric vibration energy harvesters, *AIAA Journal* 45 (5) (2007) 1126–1137.
[12] B.P. Mann, N.D. Sims, Energy harvesting from the nonlinear oscillations of magnetic levitation, *Journal of Sound and Vibration* 319 (2009) 515–530.
[13] A. Triplett, D.D. Quinn, Experimental investigation of energy harvesting with essential nonlinearities, *Proceedings of ASME IDETC/CIE 2011*, Paper No. DETC2011-48164, Washington DC, August 28–31, 2011.
[14] Y. Hu, H. Xue, J. Yang, Q. Jiang, Nonlinear behavior of a piezoelectric power harvester near resonance, *IEEE Transactions on Ultrasonics, Ferroelectrics and Frequency Control* 53 (7) (2006) 1387–1391.
[15] D. Andersen, A.F. Vakakis, Y. Starosvetsky, L.A. Bergman, Dynamic instabilities in coupled oscillators induced by geometrically nonlinear damping, *Nonlinear Dynamics* 67 (2012) 807–827.
[16] A.F. Vakakis, Inducing passive nonlinear energy sinks in linear vibrating systems,, *Journal of Vibration and Acoustics* 123 (3) (2001) 324–332.
[17] A.F. Vakakis, L.I. Manevitch, O. Gendelman, L.A. Bergman, Dynamics of linear discrete systems connected to local essentially nonlinear attachments,, *Journal of Sound and Vibration* 264 (2003) 559–577.
[18] G. Kerschen, Y. Lee, A.F. Vakakis, D.M. McFarland, L.A. Bergman, Irreversible passive energy transfer in coupled oscillators with essential nonlinearity, *SIAM Journal on Applied Mathematics* 66 (2) (2006) 648–679.
[19] D. Anderson, Y. Starosvetsky, M. Mane, S. Hubbard, K. Remick, X. Wang, A. Vakakis, L.A. Bergman, Non-resonant damped transitions resembling continuous resonance scattering in coupled oscillators with essential nonlinearities, *Physica D* 241 (2012) 964–974.
[20] A.P. Itin, A.I. Neishtadt, A.A. Vasiliev, Captures into resonance and scattering on resonance in dynamics of a charged relativistic particle in magnetic field and electrostatic wave, *Physica D* 141 (2000) 281–296.
[21] G. Kerschen, O. Gendelman, A.F. Vakakis, L.A. Bergman, D.M. McFarland, Impulsive periodic and quasi-periodic orbits of coupled oscillators with essential stiffness nonlinearity, *Communications in Nonlinear Science and Numerical Simulation* 13 (2008) 959–978.
[22] A.F. Vakakis, O. Gendelman, L.A. Bergman, D.M. McFarland, G. Kerschen, Y.S. Lee, *Nonlinear Targeted Energy Transfer in Mechanical and Structural Systems*, Springer Verlag, Berlin, New York, 2008.
[23] T.P. Sapsis, D.D. Quinn, A.F. Vakakis, L.A Bergman, Effective stiffening and dampingenhancement of structures with strongly nonlinear local attachments, *Journal of Vibration and Acoustics* 134 (1) (2012) 011016. (12 pp.).
[24] K. Remick, A.F. Vakakis, L.A. Bergman, D.M. McFarland, D.D. Quinn, T. Sapsis, Sustained high-frequency dynamic instability of a nonlinear system of coupled oscillators forced by single or repeated impulses: theoretical and experimental results, *Journal of Vibration and Acoustics* 136 (1) (2014) 011013, http://dx.doi.org/10.1115/1.4025605.
[25] N. Minorsky, *Nonlinear Oscillations*, Van Nostrand, Princeton, 1962.
[26] B. D'Urso, R. Van Handel, B. Odom, D. Hanneke, G. Gabrielse, Single-particle self-excited oscillator, *Physical Review Letters* 94 (2005) 113002.
[27] M.A. Karami, D.J. Inman, Equivalent damping and frequency change for linear and nonlinear hybrid vibrational energy harvesting systems, *Journal of Sound and Vibration* 330 (2011) 5583–5597.
[28] B.P. Mann, D.A.W. Barton, B.A.M. Owens, Uncertainty in performance for linear and nonlinear energy harvesting strategies, *Journal of Intelligent Material Systems* ; http://dx.doi.org/10.1177/1045389X12439639.
[29] A. Erturk, J. Hoffmann, D.J. Inman, A piezomagnetoelastic structure for broadband vibration energy harvesting, *Applied Physics Letters* 94 (2009) 254102.
[30] B.P. Mann, B.A. Owens, Investigations of a nonlinear energy harvester with a bistable potential well, *Journal of Sound and Vibration* 329 (2010) 1215–1226.
[31] B.P Mann, Energy criterion for potential well escapes in a bistable magnetic pendulum, *Journal of Sound and Vibration* 323 (2009) 864–876.
[32] A. Erturk, D. Inman, Broadband piezoelectric power generation on high-energy orbits of the bistable doffing oscillator with electromechanical coupling, *Journal of Sound and Vibration* 330 (2011) 2339–2353.
[33] T. Seuaciuc-Osório, M.F. Daqaq, Energy harvesting under excitations of time-varying frequency, *Journal of Sound and Vibration* 329 (2010) 2497–2515.
[34] P. Mitcheson, T. Toh, K. Wong, S. Burrow, A. Holmes, Tuning the resonant frequency and damping of an energy harvester using power electronics, *IEEE Transactions on Circuits and Systems* 58 (Part 2) (2011) 792–796.
[35] D. Barton, S. Burrow, L. Clare, Energy harvesting from vibrations with a nonlinear oscillator, *Journal of Vibration and Acoustics* 132 (2) (2010) 021009, http://dx.doi.org/10.1115/1.4000809.
[36] G. Szarka, B. Stark, S. Burrow, Review of power management for kinetic energy harvesting systems, *IEEE Transactions on Power Electronics* 27 (2012) 803–815.
[37] G. Szarka, S.G. Burrow, P. Proynov, B.H. Stark, Maximum power transfer tracking for ultra-low-power electromagnetic energy harvesters, *IEEE Transactions on Power Electronics* 29 (1) (2014) 201–212, http://dx.doi.org/10.1109/TPEL.2013.2251427.
[38] A. Cammarano, S.G. Burrow, D. Barton, A. Carrella, L.R. Clare, Tuning a resonant energy harvester using a generalized electrical load, *Smart Materials and Structures* 19 (5) (2011) 055003.